

Cite this: *Chem. Sci.*, 2021, 12, 14143 All publication charges for this article have been paid for by the Royal Society of Chemistry

# A combined computational and experimental study of methane activation during oxidative coupling of methane (OCM) by surface metal oxide catalysts†

Daniyal Kiani,  Sagar Sourav,  Israel E. Wachs \* and Jonas Baltrusaitis \*

The experimentally validated computational models developed herein, for the first time, show that Mn-promotion does not enhance the activity of the surface  $\text{Na}_2\text{WO}_4$  catalytic active sites for  $\text{CH}_4$  heterolytic dissociation during OCM. Contrary to previous understanding, it is demonstrated that Mn-promotion poisons the surface  $\text{WO}_4$  catalytic active sites resulting in surface  $\text{WO}_5$  sites with retarded kinetics for C–H scission. On the other hand, dimeric  $\text{Mn}_2\text{O}_5$  surface sites, identified and studied *via ab initio* molecular dynamics and thermodynamics, were found to be more efficient in activating  $\text{CH}_4$  than the poisoned surface  $\text{WO}_5$  sites or the original  $\text{WO}_4$  sites. However, the surface reaction intermediates formed from  $\text{CH}_4$  activation over the  $\text{Mn}_2\text{O}_5$  surface sites are more stable than those formed over the  $\text{Na}_2\text{WO}_4$  surface sites. The higher stability of the surface intermediates makes their desorption unfavorable, increasing the likelihood of over-oxidation to  $\text{CO}_x$ , in agreement with the experimental findings in the literature on Mn-promoted catalysts. Consequently, the Mn-promoter does not appear to have an essential positive role in synergistically tuning the structure of the  $\text{Na}_2\text{WO}_4$  surface sites towards  $\text{CH}_4$  activation but can yield  $\text{MnO}_x$  surface sites that activate  $\text{CH}_4$  faster than  $\text{Na}_2\text{WO}_4$  surface sites, but unselectively.

Received 17th April 2021  
Accepted 4th October 2021

DOI: 10.1039/d1sc02174e

rsc.li/chemical-science

## 1. Introduction

Methane ( $\text{CH}_4$ ) the main component of natural gas, is a sustainable energy vector and an emerging building block for synthesis of chemicals and fuels.<sup>1–5</sup> Direct  $\text{CH}_4$  conversion to ethylene ( $\text{C}_2\text{H}_4$ ) *via* oxidative coupling of methane (OCM) remains an active research frontier with ongoing studies in both catalysis science and reaction engineering.<sup>6–9</sup> Despite continued interest, the lack of the fundamental understanding of the structure–function relationships in the state-of-the-art OCM catalysts has prohibited industrial-scale application of OCM.<sup>2,10,11</sup> Recent work on selective OCM catalyst development chiefly focuses on the combinatorial screening of multicomponent mixed-phase catalyst systems as well as scrutinizing developed catalyst libraries using data science methods.<sup>7,12–14</sup> The structure–activity relationships of any catalyst, however, are the foundation for rational design and optimization of heterogeneous catalysts.<sup>15–17</sup> Under typical OCM reaction conditions ( $\text{CH}_4 + \text{O}_2$  and high temperatures of up to 850 °C), the catalytic active sites are not mere static geometric forms obtained on calcined supports but undergo dynamic rearrangement dictated

by thermodynamics.<sup>18,19</sup> Therefore, well-defined catalysts under reaction conditions should be investigated in order to understand the fundamental OCM catalyst structure–activity relationships.

Dispersed phase catalysts offer key advantages over catalysts containing a mixture of dispersed and crystalline phases,<sup>16,20–23</sup> since dispersed phase catalysts consist of atomically dispersed sites with well-defined molecular and electronic structure that can be tuned *via* the addition of promoters. Such control of the nature and the structure of catalytic active sites remains challenging in the presence of a crystalline phase in supported mixed phase catalysts, which exhibit an ensemble distribution of the catalytic active sites distributed in the various phases, hence complicating the structure–activity analysis. This difference in dispersed *vs.* mixed phase catalysts is illustrated in Fig. 1 using silica ( $\text{SiO}_2$ ) supported metal oxide ( $\text{MO}_x$ ) catalysts, such as those used for OCM, with well-defined active sites found in dispersed phase catalysts allowing systematic analysis for structure–activity relationships, and supported mixed oxide phase catalysts resulting in a variety of various types of sites.

The structure–activity relationships for the state-of-the-art supported Mn– $\text{Na}_2\text{WO}_4/\text{SiO}_2$  tri-metal oxide OCM catalyst have remained elusive not only due to the demanding reaction conditions, but also due to the mixed-oxide phase nature of this catalyst.<sup>24</sup> While dispersed phase tri-metal oxide catalysts, *i.e.*, containing all three metal oxides (W, Na, Mn), have not been studied to date, the structure–activity relationships of active

Department of Chemical and Biomolecular Engineering, Lehigh University, B336 Iacocca Hall, 111 Research Drive, Bethlehem, PA 18015, USA. E-mail: job314@lehigh.edu; iew0@lehigh.edu

† Electronic supplementary information (ESI) available. See DOI: 10.1039/d1sc02174e



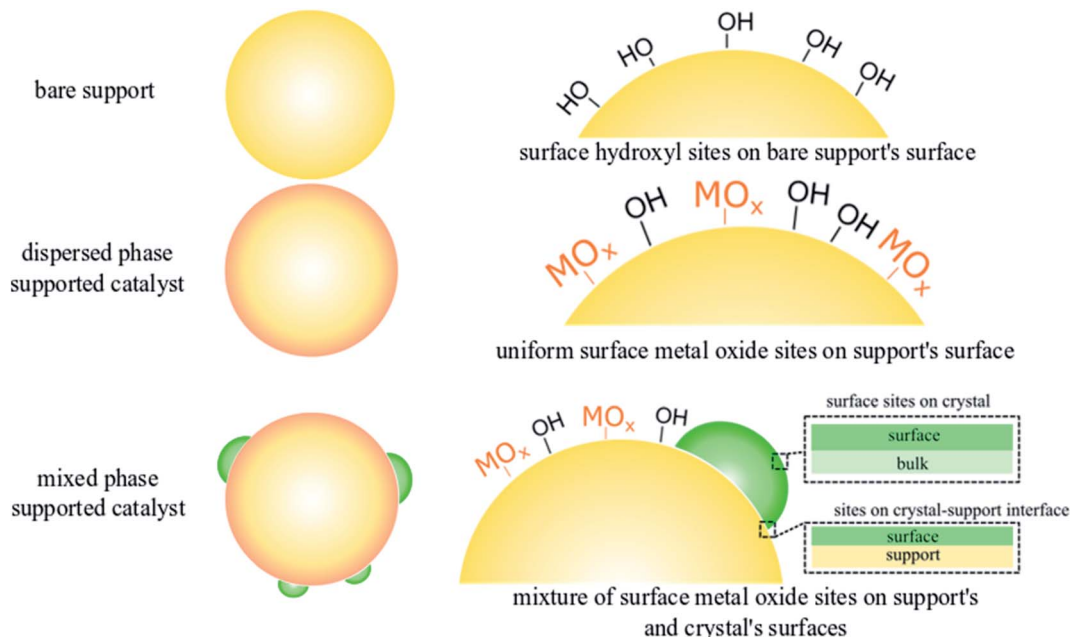


Fig. 1 The nature and type of surface sites on  $\text{SiO}_2$  support, dispersed and mixed-phase supported tungsten oxide catalysts used in OCM. The support contains surface hydroxyls ( $-\text{OH}$ ) where the active metal oxides ( $\text{MO}_x$ , such as  $\text{WO}_x$ ,  $\text{MnO}_x$ ) anchor in dispersed phase catalysts. For the supported mixed-oxide phase catalysts, the dispersed phase metal oxide anchors onto the surface  $-\text{OH}$  sites of the support and the crystalline phase is also present resulting in a wide range of metal oxide sites, along with those present at the interface of the crystal-support.

sites in dispersed phase bi-metal oxide catalysts ( $\text{Na}-\text{WO}_x/\text{SiO}_2$ ,  $\text{Mn}-\text{WO}_x/\text{SiO}_2$ ) for OCM have been recently reported.<sup>22,25</sup> It was shown that the distorted surface  $\text{WO}_4$  sites are present at elevated temperatures (673 K) on the amorphous  $\text{SiO}_2$  surface in unpromoted, supported  $\text{WO}_x/\text{SiO}_2$  catalysts.<sup>22</sup> Upon Na-promotion, the extent of distortion of the  $\text{WO}_4$  surface site diminishes.<sup>22,25</sup> The dispersed-phase Na-coordinated  $\text{WO}_4$  surface sites ( $\text{Na}-\text{WO}_4$ ) with Na/W molar ratio less than 2 were shown to be significantly more selective to  $\text{C}_2$  products than the unpromoted, surface  $\text{WO}_4$  sites and the corresponding mixed-oxide phase catalysts containing crystalline phase  $\text{Na}_2\text{WO}_4$  ( $\text{Na}/\text{W} \sim 2$ ).<sup>22,25</sup> Moreover, the promotion with Mn *i.e.*  $\text{Mn}-\text{WO}_x/\text{SiO}_2$ , did not have a significant impact on the molecular structure and OCM  $\text{C}_2$  selectivity of the  $\text{WO}_4$  surface sites in comparison to unpromoted  $\text{WO}_4$  surface sites.<sup>25</sup> Thus, the role of Mn for the OCM catalytic reaction remains unclear.

Older studies of mixed-phase tri-metal oxide catalysts under/near OCM reaction conditions revealed that  $\text{Mn}^{3+}$  reduces to  $\text{Mn}^{2+}$  during  $\text{CH}_4$  activation, which can then be re-oxidized to  $\text{Mn}^{3+}$  during the second half of the OCM reaction redox cycle.<sup>26</sup> Based on the proposed  $\text{Mn}^{3+} \rightarrow \text{Mn}^{2+} \rightarrow \text{Mn}^{3+}$  redox cycle, multiple reaction models suggesting Mn sites as the catalytic active site during OCM have been put forth in the literature.<sup>26-29</sup> Note that the observed redox cycle, however, was purely based on transitions observed in the crystalline phases of manganese oxide ( $\text{Mn}_2\text{O}_3$  and  $\text{Mn}_3\text{O}_4$ ) and the redox behavior of the dispersed phase manganese oxide surface sites ( $\text{MnO}_x$ ) in the catalyst are still not known. More recently, an *operando* synchrotron  $\mu\text{-XRF/XRD}$ /absorption-computed tomography investigation of the mixed-phase tri-metal oxide catalyst found

that during phase transformations occurring in the crystalline manganese oxide phases ( $\text{Mn}_2\text{O}_3$ ,  $\text{Mn}_7\text{SiO}_{12}$  and  $\text{MnWO}_4$ ), product distribution did not change. Hence, it was concluded that such manganese oxide phases did not have a critical role in the catalytic OCM reaction.<sup>30</sup> It was further concluded that dispersed phase  $\text{MnO}_x$  surface sites present on the  $\text{SiO}_2$  support in the mixed-phase tri-metal oxide catalyst, which bulk X-ray based techniques such as XRD, XAS, XRF cannot effectively monitor, may be involved in the OCM catalytic cycle.<sup>30</sup>

Herein, we provide the first *in silico* framework validated with *in situ* spectroscopy measurements to study the structure-activity relationship of metal oxide sites in model tri-metal oxide OCM catalysts containing Mn, W, Na metal oxides on a  $\text{SiO}_2$  support. In particular, the nature and structure of the tri-metal oxide surface sites ( $\text{Mn}-\text{Na}_2\text{WO}_4/\text{SiO}_2$ ) was elucidated and contrasted with the bi-metal oxide surface sites ( $\text{Na}_2\text{WO}_4$ ) *via ab initio* molecular dynamics (AIMD) and periodic density functional theory (DFT).  $\text{Na}_2\text{WO}_4$  surface sites are used as the base for this comparison as these surface sites were shown to be the selective active sites for  $\text{CH}_4$  activation during OCM.<sup>19,22,25</sup> The DFT predicted molecular and electronic structures of the dispersed phase surface sites in bi- and tri-metal oxide OCM catalyst prior to  $\text{CH}_4$  activation were also validated by *in situ* Raman and *in situ* UV-Vis diffused reflectance (UV-VisDR) spectroscopies at dehydrated oxidative conditions (400 °C, 10%  $\text{O}_2$ /inert), respectively. Intrinsic kinetics of  $\text{CH}_4$  dissociation over surface sites in dispersed phase bi-metal oxide and tri-metal oxide case were calculated and contrasted. Results herein provide molecular-level insights on the nature of surface sites, and their activity towards heterolytic  $\text{CH}_4$  dissociation during



OCM, providing structure–function relationships for this OCM catalyst.

## 2. Experimental

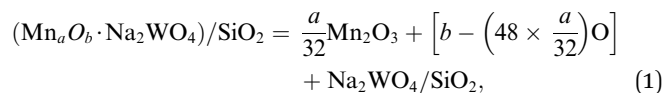
### (a) Computational modelling

The periodic calculations have been performed with the Vienna *Ab Initio* Simulation package (VASP) using the Perdew and Wang (PW91) generalized gradient approximation exchange–correlation functional. PW91 exchange–correlation functional is used as model used herein are adapted from prior models of supported  $\text{WO}_x$  catalysts published in the literature.<sup>25,31,32</sup> The valence electrons are treated explicitly and their interactions with the ionic cores are described by the Projector Augmented-Wave method (PAW), which allows using low energy cut off equal to 400 eV for the plane-wave basis. A sampling of the Brillouin zone with  $2 \times 2 \times 1$  mesh was applied for all models in this work. The positions of the two top-most layer surface slab atoms, as well as the active (un)coordinated  $\text{WO}_x$  site, in the supercell, were relaxed until the total energy differences decrease below  $10^{-6}$  eV (forces acting on atoms fall below  $0.005 \text{ eV } \text{\AA}^{-1}$ ). The details of the model of the hydroxylated  $\beta$ -cristobalite slab can be found elsewhere.<sup>25</sup>

Vibrational modes have been calculated for the selected surface species within the harmonic approximation. Only the tungsten active center and its 1st and 2nd neighbors (O–Si and OH groups) were considered in the Hessian matrix. This matrix was computed by the finite difference method followed by a diagonalization procedure. The eigenvalues of the resulting matrix led to frequency values. The assignment of the vibrational modes was done by inspection of the corresponding eigenvectors. Static (NSW = 0, IBRION = -1) self-consistent calculations were performed to compute DOS (ISMAR = 0, Sigma = 0.02), and the resulting vasprun.xml files were visualized using P4Vasp<sup>33,34</sup> to extract local and total density of states (LDOS, total DOS).

*Ab initio* molecular dynamics (AIMD) calculations were performed using Anderson thermostat (1700 K, 2 fs steps) to provide sufficient kinetic energy to the simulated catalyst surface for the atoms to rearrange so the global minima for the total energy can be calculated. The antiferromagnetic configuration in dimeric  $\text{Mn}_2\text{O}_x$  cases was consistently lower in energy than ferromagnetic configurations, so all dimeric  $\text{Mn}_2\text{O}_x$  studied here were treated as antiferromagnetic. Typically, ~8000 fs AIMD simulations resulted in 3–4 lowest energy structures, which were then extracted and further optimized by periodic DFT before subsequent calculations were conducted for frequencies, Bader<sup>35</sup> charges and transition states (from nudged elastic band (NEB)<sup>36,37</sup>) on the lowest energy structure amongst the 3–4 selected from AIMD. *Ab initio* thermodynamics (AITD) were calculated according to the framework described in the recent literature.<sup>13,38–40</sup> Specifically, the relative stability of various possible surface  $\text{Mn}_a\text{O}_b$  clusters were computed in reference to the bulk  $\alpha$ - $\text{Mn}_2\text{O}_3$  phase (unit cell: 32Mn atoms, 48O atoms),<sup>41</sup> which is typically reported to be stable under OCM relevant conditions ( $T = 1000 \text{ K}$ ,  $P_{\text{O}_2} = 0.33\text{--}0.1$ ).<sup>42</sup> The  $\text{Mn}_2\text{O}_3$  atom positions and cell parameters were relaxed with

high precision and cutoff energy of 520 eV to minimize any Pulay stress. Given the unit cell of  $\alpha$ - $\text{Mn}_2\text{O}_3$  containing 32Mn and 48O atoms, the general governing stoichiometric equation can be written as (1)



with the overall exergonicity or endergonicity of the reaction to form isolated  $\text{Mn}_a\text{O}_b$  clusters, rather than bulk  $\text{Mn}_2\text{O}_3$ , on  $\text{Na}_2\text{WO}_4/\text{SiO}_2$  described *via* (2)

$$\Delta G(T, P) = \mu((\text{Mn}_a\text{O}_b \cdot \text{Na}_2\text{WO}_4)/\text{SiO}_2) - \frac{a}{32}\mu(\text{Mn}_2\text{O}_3) - \left[ b - \left( 48 \times \frac{a}{32} \right) \right] \mu(\text{O}) - \mu(\text{Na}_2\text{WO}_4/\text{SiO}_2). \quad (2)$$

In this method, the PV contributions of solids were neglected,<sup>13,38–40</sup> and the Gibbs free energies of solids were approximated as their respective electronic energies computed by DFT with thermal corrections in accordance with the methodology described in the literature,<sup>43</sup> as shown in eqn (3)

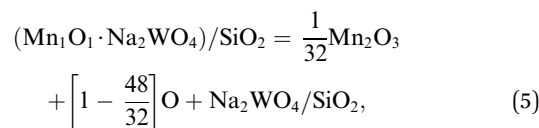
$$\mu(\text{solid}) = E_{0\text{K}}^{\text{DFT}}(\text{solid}) + G_{\text{vib}}(T). \quad (3)$$

The chemical potential of the gas phase  $\text{O}_2$  depends on the temperature ( $T$ ) and the corresponding partial pressure ( $P$ ). At arbitrary  $T$  and  $P$ ,  $\mu_{\text{O}_2}$  can then be written as:

$$\mu_{\text{O}_2}(T, P) = E_{\text{O}_2}^{\text{DFT}} + E_{\text{O}_2}^{\text{ZPE}} + \Delta\mu(T, P^\circ) + RT \ln(P/P^\circ) \quad (4)$$

here,  $R$  is the gas constant, 300 K is the reference  $T$ , and 1 atm (101 325 Pa;  $P/P^\circ = 1$ ) is the reference pressure.  $\Delta\mu(T, P^\circ)$  were taken from JANAF tables.<sup>44</sup>  $E_{\text{O}_2}^{\text{DFT}}$  was the DFT calculated energy of  $-9.81 \text{ eV}$  and  $E_{\text{O}_2}^{\text{ZPE}}$  value is  $0.098 \text{ eV}$ .<sup>45</sup>  $\mu_{\text{O}}$  (*i.e.*  $\frac{1}{2}\mu_{\text{O}_2}$ ) values calculated as a function of  $T$  and  $P$  are tabulated and plotted in Table S1 and Fig. S1,<sup>†</sup> respectively, and agree with those reported in the literature.<sup>46,47</sup> Thus, Gibbs free energy of formation ( $G_{\text{form}}$ ) for a specific case can be written as eqn (2), where  $\mu(\text{Na}_2\text{WO}_4/\text{SiO}_2)$ ,  $\mu(\text{Mn}_a\text{O}_b + \text{Na}_2\text{WO}_4/\text{SiO}_2)$ , and  $\mu(\text{Mn}_2\text{O}_3)$  are chemical potentials of the solid phases calculated according to eqn (3), while  $\mu_{\text{O}}$  is the oxygen chemical potential calculated according to eqn (4).

For example, using the general eqn (1), the  $\text{Mn}_1\text{O}_1\text{--Na}_2\text{WO}_4/\text{SiO}_2$  system was calculated as:



with

$$\Delta G(T, P) = \mu(\text{Mn}_1\text{O}_1 \cdot \text{Na}_2\text{WO}_4/\text{SiO}_2) - \left( \frac{1}{32}\mu(\text{Mn}_2\text{O}_3) - \frac{1}{2}\mu_{\text{O}} + \mu(\text{Na}_2\text{WO}_4/\text{SiO}_2) \right). \quad (6)$$

Using eqn (1), the comprehensive  $\text{Mn}_a\text{O}_b$  chemical potential landscape was computed for various mono-atomic (Mn, MnO,  $\text{MnO}_2$ ,  $\text{MnO}_3$ ) and di-atomic ( $\text{Mn}_2\text{O}$ ,  $\text{Mn}_2\text{O}_2$ ,  $\text{Mn}_2\text{O}_3$ ,  $\text{Mn}_2\text{O}_4$ ,



Mn<sub>2</sub>O<sub>3</sub> compositions to compare their respective thermodynamic stability given OCM relevant conditions of 1000 K and  $P_{\text{O}_2}/P^{\circ}$  of 0.1–0.33. A higher degree of oligomerization for surface Mn<sub>a</sub>O<sub>b</sub> compositions was not considered due to the complexity of the possible structures in tri- and tetra-atomic cases such as straight 2D-chain vs. 3D-clusters.

Lastly, intrinsic rate constant ( $k_{\text{d}}^{\circ}$ ) of C–H dissociation in CH<sub>4</sub> was calculated using the DFT-computed  $E_0$  values of transition states identified *via* NEB method, according to equation:

$$k_{\text{d}}^{\circ}(\text{s}^{-1}) = \frac{k_{\text{B}} T}{h} e^{-\frac{E_{\text{a}}}{RT}}, \quad (7)$$

where  $k_{\text{B}}$  is the Boltzmann constant (J K<sup>-1</sup>),  $h$  is the Planck's constant (J s),  $T$  is the reaction temperature (K),  $R$  is the gas constant (J K<sup>-1</sup> mol<sup>-1</sup>), and  $E_{\text{a}}$  is the energy difference with  $E_0$  values of initial and transition state structures in J mol<sup>-1</sup>.

### (b) Non-stoichiometric catalyst synthesis

The SiO<sub>2</sub> support (Cabot CAB-O-SIL® EH5 with a surface area of ~332 m<sup>2</sup> g<sup>-1</sup>) was first treated with water, then allowed to dry overnight at room temperature before final calcination at 500 °C for 4 hours under flowing air. This treatment increases the density and surface hydroxyls of the SiO<sub>2</sub> support. The dried SiO<sub>2</sub> obtained after calcination was then crushed into a fine powder. The resulting pore volume of the SiO<sub>2</sub> powder was determined to be ~0.8 mL g<sup>-1</sup> and was utilized for all catalyst preparation steps *via* incipient-wetness impregnation (IWI) of the metal oxide aqueous solutions unless mentioned otherwise. A NaOH aqueous solution corresponding to the pore-volume equivalent of ~0.8 mL g<sup>-1</sup> was impregnated onto the SiO<sub>2</sub> support and the sample was initially dried overnight, then at 120 °C in an oven under flowing air for 2 hours, and finally calcined at 700 °C under airflow for 2 hours. The resultant supported Na/SiO<sub>2</sub> sample, with pore volume equivalent of ~0.7 mL g<sup>-1</sup>, was subsequently impregnated with the desired aqueous concentration of W in the form of AMT ((NH<sub>4</sub>)<sub>x</sub>W<sub>12</sub>O<sub>28</sub>; Alfa Aesar, #44792) and Mn in the form of Mn(NO<sub>3</sub>)<sub>2</sub> (Alfa Aesar, #10806-09). The resultant solid was dried overnight, then at 120 °C for 2 hours in airflow and finally calcined at 500 °C for 4 hours under flowing air. The final catalysts were denoted as 8% W/0.4%Na/SiO<sub>2</sub> (Na/W = 0.4)<sup>22</sup> in the bi-metal oxide case and 0.5%Mn–8%W/0.4%Na/SiO<sub>2</sub> (Na/W = 0.4, Mn/W = 0.2) in the tri-metal oxide case. Samples calcined at 500 °C calcination did not undergo sintering typical of higher temperature calcination, enabling easier characterization of the surface metal oxide sites, which becomes challenging in low surface area sintered materials.

### (c) *In situ* Raman spectroscopy

The *in situ* Raman spectra of the Na coordinated WO<sub>x</sub>/SiO<sub>2</sub> supported catalysts were obtained with Horiba-Jobin Yvon LabRam HR instrument equipped with three laser excitations (532, 442, and 325 nm) and liquid N<sub>2</sub>-cooled CCD detector (Horiba-Jobin Yvon CCD-3000 V). The 442 nm laser was chosen for spectral accumulation since it minimizes sample fluorescence from the SiO<sub>2</sub> supported catalysts. The wavenumber

calibration was checked using a standard silicon wafer with a Raman vibration at 520.7 cm<sup>-1</sup>. A confocal microscope with a 50× objective (Olympus BX-30-LWD) was utilized for focusing the laser on the catalysts. Typically, the spectra were collected for 60 s per scan for a total of three scans with a 1000 μm hole with a spectral resolution of ~1 cm<sup>-1</sup>. Approximately 15–20 mg of each catalyst in powder form (100–150 μm size range) was loaded into an environmental cell (Linkam CCR-1000) with a quartz window with O-ring seals, which was kept cool by circulating cooling water. The *in situ* Raman spectra of the catalysts were collected at 400 °C after dehydration in 10% O<sub>2</sub>/Ar (~30 cc min<sup>-1</sup>) for 60 min to elucidate the initial molecular structure of the representative bi- and tri-metal oxide surface sites to validate the DFT-optimized structures before reaction with CH<sub>4</sub>.

### (d) *In situ* UV-Vis DR spectroscopy

The *in situ* UV-Vis spectra of the catalysts were obtained using a Varian Cary 5E UV-Vis-NIR spectrophotometer with a Harrick Praying Mantis accessory. Approximately 15–20 mg of each catalyst in powder form was loaded into an *in situ* Harrick HVCDR2 environmental cell. The UV-Vis spectra of the catalyst samples were collected at 400 °C in the 200–800 nm wavelength range after dehydration (10% O<sub>2</sub>/Ar, ~30 cc min<sup>-1</sup>) for 60 min, using a scan rate of 15 nm min<sup>-1</sup> and a signal averaging time of 0.6 s. MgO was used as a standard for obtaining the background absorbance and was subtracted from the sample absorbance. Kubelka–Munk function  $F(R_{\infty})$  was calculated from the background-subtracted absorbance data of the UV-Vis spectrum of each sample. The edge energy ( $E_{\text{g}}$ ), or bandgap, was determined by finding the intercept of the straight line for the low-energy rise of a plot of  $[F(R_{\infty})/hv]^2$  versus  $hv$ , where  $hv$  is the incident photon energy. The *in situ* UV-Vis spectra of the catalysts at 400 °C after dehydration in 10% O<sub>2</sub>/Ar were used to elucidate the initial electronic structure of the representative bi- and tri-metal oxide surface sites to validate the DFT-optimized structures before reaction with CH<sub>4</sub>.

## 3. Results and discussion

### (a) Thermodynamic stability of Mn<sub>a</sub>O<sub>b</sub>–Na<sub>2</sub>WO<sub>4</sub>/SiO<sub>2</sub> catalysts under OCM relevant conditions

The Gibbs free energies of formation ( $\Delta G(T, P)$  further referred to as  $\Delta G_{\text{form}}$ ) of Mn<sub>a</sub>O<sub>b</sub> surface sites in Na<sub>2</sub>WO<sub>4</sub>/SiO<sub>2</sub> catalysts were computed as a function of oxygen partial pressure according to eqn (2) with respect to the bulk Mn<sub>2</sub>O<sub>3</sub> phase. In an oxygen containing reaction mixture, the surface Mn<sub>a</sub>O<sub>b</sub> sites are expected to be oxidized depending on the partial pressure of the oxygen. Therefore, as a starting point,  $\Delta G_{\text{form}}$  was computed for four possible mono-atomic Mn<sub>1</sub>O<sub>b</sub> cases Mn, MnO, MnO<sub>2</sub>, and MnO<sub>3</sub>, where  $b$  is 0, 1, 2 and 3, respectively. As shown in the heat maps in Fig. 2a–d, the redder tones signify positive values of  $\Delta G_{\text{form}}$  and bluer tones signify negative  $\Delta G_{\text{form}}$ . Positive  $\Delta G_{\text{form}}$  imply that formation of that cluster is endergonic with respect to bulk Mn<sub>2</sub>O<sub>3</sub>, while negative values imply that the formation of that cluster is exergonic with respect to bulk Mn<sub>2</sub>O<sub>3</sub>. Fig. 2a–



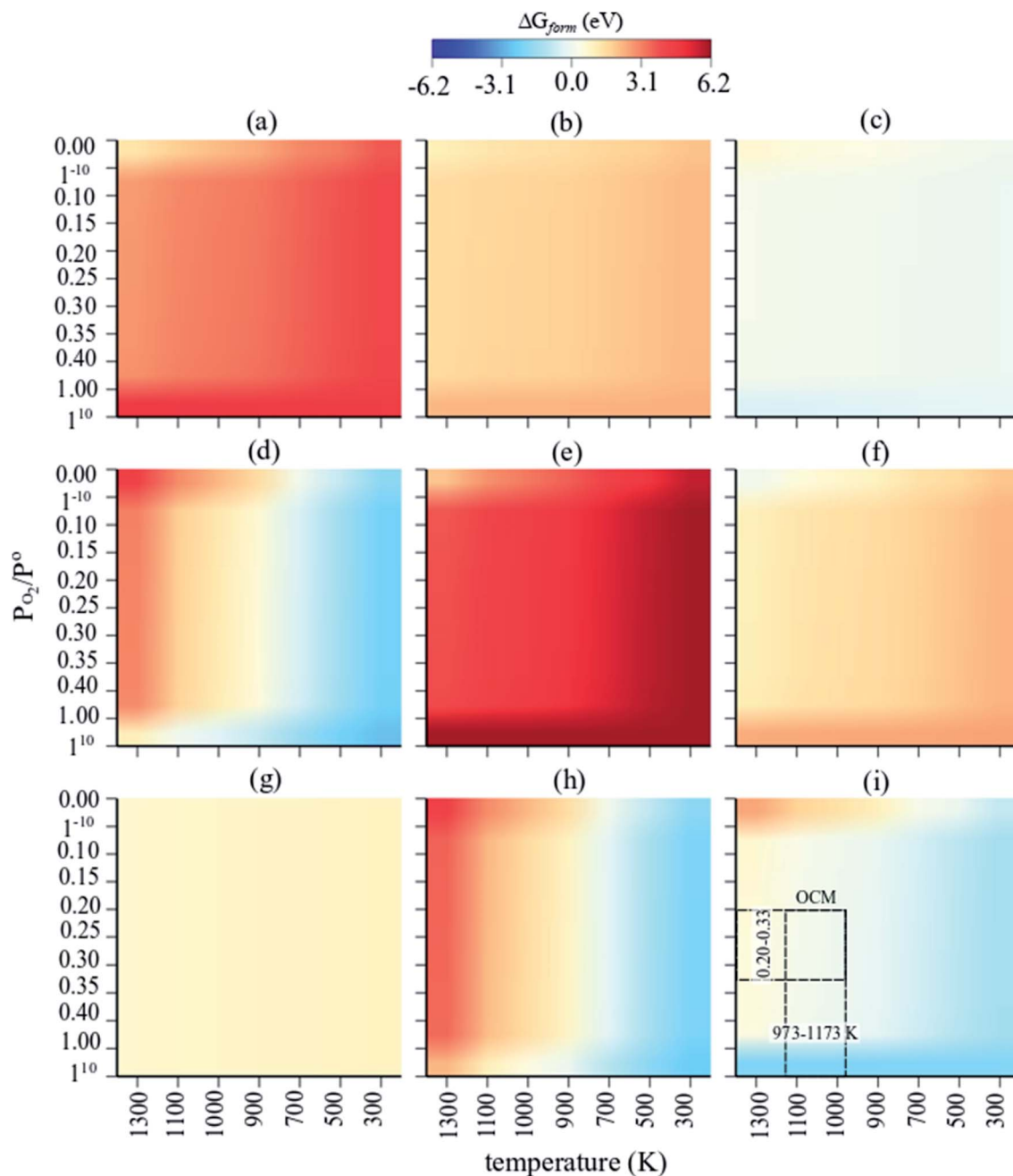


Fig. 2 Individual heat maps of computed Gibbs free energy of formation for  $(\text{Mn}_3\text{O}_b\text{-Na}_2\text{WO}_4)/\text{SiO}_2$  as a function of  $T$  (300–1300 K) and  $P_{\text{O}_2}/P = 0-1$  (ref. 10) for (a) Mn, (b) MnO, (c)  $\text{MnO}_2$ , (d)  $\text{MnO}_3$ , (e)  $\text{Mn}_2\text{O}$ , (f)  $\text{Mn}_2\text{O}_2$ , (g)  $\text{Mn}_2\text{O}_3$ , (h)  $\text{Mn}_2\text{O}_4$ , (i)  $\text{Mn}_2\text{O}_5$ . The dashed rectangle in (i) signifies the OCM relevant conditions.

d show that the formation of isolated Mn, MnO,  $\text{MnO}_3$  surface sites are clearly endergonic in comparison to bulk  $\text{Mn}_2\text{O}_3$  under OCM conditions ( $\sim 973-1173$  K,  $P_{\text{O}_2}/P = 0.20-0.33$ ). However, the isolated  $\text{MnO}_2$  formation is barely endergonic relative to bulk  $\text{Mn}_2\text{O}_3$  under OCM conditions and in fact becomes exergonic at high  $P_{\text{O}_2}$  and low temperatures. Likewise, five stoichiometries possible considered for the di-atomic  $\text{Mn}_2\text{O}_b$  are  $\text{Mn}_2\text{O}$ ,  $\text{Mn}_2\text{O}_2$ ,  $\text{Mn}_2\text{O}_3$ ,  $\text{Mn}_2\text{O}_4$ , and  $\text{Mn}_2\text{O}_5$  where  $b$  is 1, 2, 3, 4, and 5 respectively. The computed  $\Delta G_{\text{form}}$  for each case are shown as heat maps in Fig. 2e–i. At OCM conditions, besides

$\text{Mn}_2\text{O}_5$ , the formation of di-atomic sites ( $\text{Mn}_2\text{O}$ ,  $\text{Mn}_2\text{O}_2$ ,  $\text{Mn}_2\text{O}_3$ ,  $\text{Mn}_2\text{O}_4$ ) is endergonic in reference to the bulk  $\text{Mn}_2\text{O}_3$  and thus unfavorable. Therefore, under OCM conditions, formation of  $\text{Mn}_2\text{O}_5$  sites yielding  $\text{Mn}_2\text{O}_5\text{-Na}_2\text{WO}_4/\text{SiO}_2$  catalyst the most thermodynamically favorable from an AITD standpoint.

In a comparison shown in Fig. 3, the entire catalyst structure space of  $\text{Mn}_a\text{O}_b\text{-Na}_2\text{WO}_4/\text{SiO}_2$  was compared to ascertain the most thermodynamically stable stoichiometry of surface  $\text{Mn}_a\text{O}_b$  sites in  $\text{Mn}_a\text{O}_b\text{-Na}_2\text{WO}_4/\text{SiO}_2$  catalysts under OCM relevant  $P_{\text{O}_2}/P^0$  of 0.2–0.33, and temperature of 1000 K. Under these



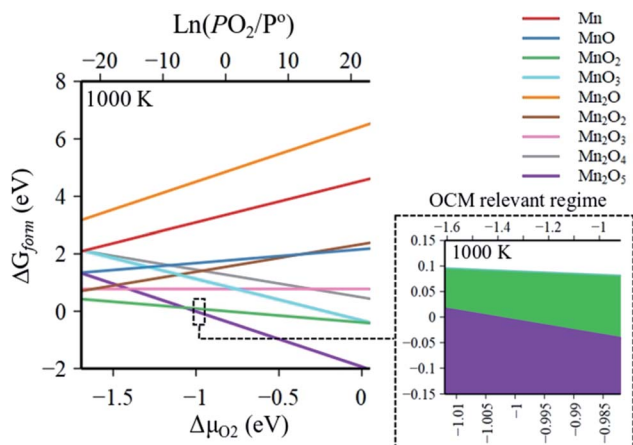


Fig. 3 Global comparison of Gibbs free energy of formation of  $(\text{Mn}_a\text{O}_b-\text{Na}_2\text{WO}_4)/\text{SiO}_2$  at OCM relevant conditions ( $P_{\text{O}_2}/P^\circ = 0.20-0.33$  at 1000 K) identifying  $\text{Mn}_2\text{O}_5-\text{Na}_2\text{WO}_4/\text{SiO}_2$  as the most thermodynamically stable structure under these conditions.

conditions, the formation of  $\text{Mn}_2\text{O}_5$  dimeric sites is evidently thermodynamically favorable (*i.e.* most exergonic) with reference to bulk  $\text{Mn}_2\text{O}_3$ , especially towards  $P_{\text{O}_2}/P^\circ$  values  $\sim 0.30-0.33$  that represent the OCM reaction stoichiometry *i.e.*  $\text{CH}_4 : \text{O}_2 = 2 : 1$ . For instance, as the  $P_{\text{O}_2}/P^\circ$  values increase from 0.25 to 0.35, the  $\Delta G_{\text{form}}$  of  $\text{Mn}_2\text{O}_5$  sites decreases from  $-0.002$  eV ( $-0.20$  kJ mol $^{-1}$ ) to  $-0.031$  eV ( $-3.00$  kJ mol $^{-1}$ ). Note that since the Gibbs energy difference is so small between  $\text{MnO}_2$  and  $\text{Mn}_2\text{O}_5$ , a minor presence of  $\text{MnO}_2$  sites cannot be precluded under OCM conditions in the catalyst. However, for simplicity, the  $\text{Mn}_2\text{O}_5-\text{Na}_2\text{WO}_4/\text{SiO}_2$  catalyst was chosen for further study presented in the next sections. Specifically, the molecular and electronic structure of the surface sites in  $\text{Mn}_2\text{O}_5-\text{Na}_2\text{WO}_4/\text{SiO}_2$

catalyst are calculated and compared against the base case of unpromoted  $\text{Na}_2\text{WO}_4/\text{SiO}_2$  to ascertain the effect of Mn promotion. The base case *i.e.*  $\text{Na}_2\text{WO}_4/\text{SiO}_2$  contains Na-coordinated  $\text{WO}_4$  surface sites that have been shown to be the selective active sites for OCM in such bi-metal oxide catalysts.<sup>22,25</sup> Moreover, the molecular and electronic structures of DFT-optimized structures are also validated against experimental *in situ* characterization data to ensure agreement. Lastly,  $\text{CH}_4$  activation pathways and intrinsic kinetics are also compared in each case to elucidate the role of surface Mn sites in OCM.

### (b) Molecular structure of surface sites in $\text{Na}_2\text{WO}_4/\text{SiO}_2$ and $\text{Mn}_2\text{O}_5-\text{Na}_2\text{WO}_4/\text{SiO}_2$

The DFT-optimized molecular structure of surface sites in  $\text{Na}_2\text{WO}_4/\text{SiO}_2$  and  $\text{Mn}_2\text{O}_5-\text{Na}_2\text{WO}_4/\text{SiO}_2$  are shown in Fig. 4a. In the case of  $\text{Na}_2\text{WO}_4/\text{SiO}_2$ , bi-grafted, dioxo  $\text{WO}_4$  surface site is present in a distorted  $T_d$  geometry, in agreement with experimental and computational work previously reported in the literature.<sup>22,25</sup> On the other hand, the molecular structure of  $\text{Mn}_2\text{O}_5-\text{Na}_2\text{WO}_4/\text{SiO}_2$  contains surface  $\text{WO}_x$  site that changes dramatically in terms of its molecular structure due to interaction with the surface  $\text{Mn}_2\text{O}_5$  dimer. In this case, the bi-grafted, di-oxo  $\text{WO}_x$  is coordinated to the adjacent  $\text{Mn}_2\text{O}_5$  site *via* a single W-O-Mn bond, and so can be regarded as  $\text{WO}_5$ . The  $\text{Mn}_2\text{O}_5$  is present as a dimer bridged *via* a single Mn-O-Mn bond with both  $\text{MnO}_4$  units present as distorted pseudo tetrahedral ( $T_d$ ).

Fundamental frequencies for each case were computed and contrasted with experimental *in situ* Raman spectra of representative dehydrated catalysts to validate the computational model against experimentally observed structures, as shown in Fig. 4b and c. In each case, the computed fundamental modes

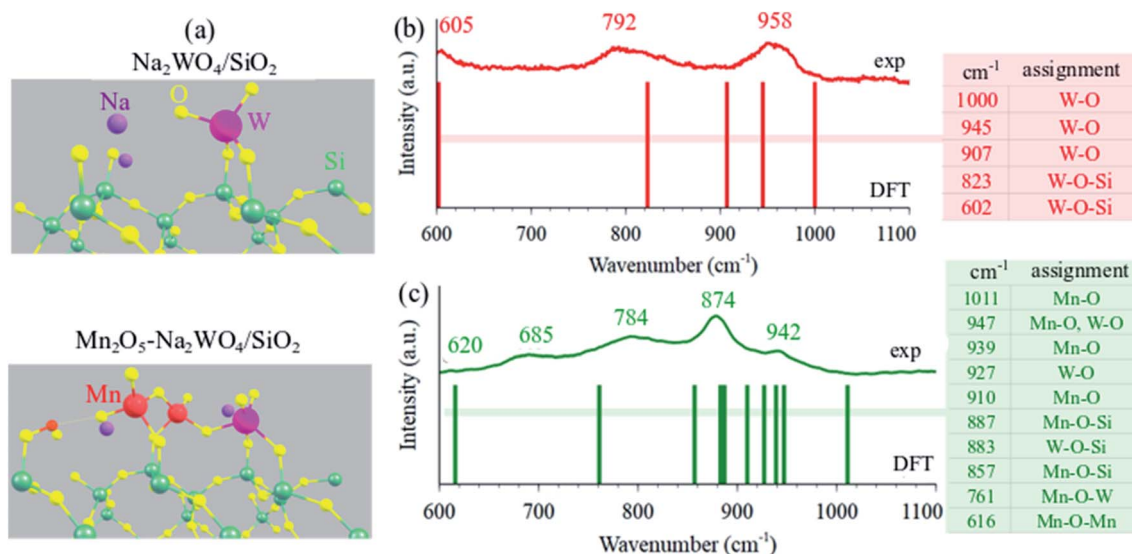


Fig. 4 (a) Periodic DFT optimized structures minimum energy structures for  $\text{Na}_2\text{WO}_4/\text{SiO}_2$  and  $\text{Mn}_2\text{O}_5-\text{Na}_2\text{WO}_4/\text{SiO}_2$  catalysts. Comparison of experimental *in situ* dehydrated Raman (400 °C, 10%  $\text{O}_2/\text{N}_2$ , 532 nm) and DFT calculated frequencies from 600–1200  $\text{cm}^{-1}$  for (b)  $\text{Na}_2\text{WO}_4/\text{SiO}_2$  and (c)  $\text{Mn}_2\text{O}_5-\text{Na}_2\text{WO}_4/\text{SiO}_2$  OCM catalysts. The vibrations from  $\text{SiO}_2$  support are not shown/labelled herein for clarity. The presence of poorly crystalline Mn- $\text{WO}_3$  and  $\text{MnWO}_4$  nanoparticles is inferred as well from the experimental *in situ* Raman spectrum in (c).



are assigned in the color-coded tables in Fig. 4b and c and the solid bars are the DFT-calculated frequencies. In both cases, general agreement is observed between computed frequencies and experimentally measured Raman bands, validating the DFT-optimized structural models. From this comparison, it is inferred that W=O bonds are the shortest, given they vibrate in the 945–1000  $\text{cm}^{-1}$  range. Likewise, support-grafting bonds like W–O–Si and Mn–O–Si are significantly longer, given they vibrate in the 800–900  $\text{cm}^{-1}$  range. Lastly, bridging bonds like Mn–O–Mn and Mn–O–W are the longest (weakest), since they vibrate at 616 and 761  $\text{cm}^{-1}$ , respectively. It should be noted that we infer a small presence of poorly crystalline nanoclusters/nanoparticles of  $\text{MnWO}_4$  and Mn-contaminated  $\text{WO}_3$  in the experimental Raman spectrum of the tri-metal oxide catalyst shown in Fig. 4c, which exhibit Raman bands in the same region as dispersed phase sites. However, since *operando/in situ* characterization studies in the literature suggest that crystalline  $\text{MnWO}_4$  is not critical to OCM,<sup>29,30</sup> and because the nature (size, shape, surface structure, defect density) of these nanoparticles is not known presently, the nanoparticles have been excluded from this computational model and only the dispersed phase surface sites were studied for structure–function relationships towards  $\text{CH}_4$  activation. Interested readers are directed to a recent, fully experimental study, where further detailed

experimental characterization including UV-VisDRS, Raman at 400 °C, Raman during OCM at 900 °C, TPSR, *etc.* of several model OCM catalysts including the two catalysts compared in Fig. 4b and c can be found.<sup>48</sup>

### (c) Electronic structure of surface sites in $\text{Na}_2\text{WO}_4/\text{SiO}_2$ and $\text{Mn}_2\text{O}_5\text{-Na}_2\text{WO}_4/\text{SiO}_2$

Next, the electronic structure of the DFT-optimized models is studied. The calculated Bader charges as well as the bond lengths are shown in Fig. 5a and b for  $\text{Na}_2\text{WO}_4/\text{SiO}_2$  and  $\text{Mn}_2\text{O}_5\text{-Na}_2\text{WO}_4/\text{SiO}_2$  cases, respectively. In both cases, the W centers have an identical Bader charge of +2.51, which corresponds to an oxidation state of +6 according to the calibration curves shown in Fig. S2,<sup>†</sup> generated according to literature reported methodology.<sup>49</sup> On the other hand, the calculated Bader charges for the two Mn atoms in  $\text{Mn}_2\text{O}_5\text{-Na}_2\text{WO}_4/\text{SiO}_2$  catalyst were +1.66 and +1.63, respectively, corresponding to an oxidation state of  $\sim +3$  (Fig. S2<sup>†</sup>), which agrees well with the literature reported Mn oxidation state of +3 under oxidative conditions (*i.e.* no  $\text{CH}_4$  at elevated temperatures).<sup>26</sup> Experimental *in situ* UV-Vis DRS was conducted on two representative samples, namely bi-metal oxide  $\text{Na-WO}_x/\text{SiO}_2$  with Na/W = 0.4, and tri-metal oxide  $\text{Mn-Na-WO}_x/\text{SiO}_2$  with Na/W = 0.4, Mn/W = 0.5 as shown in Fig. 5d. In both cases, ligand to metal charge transfer

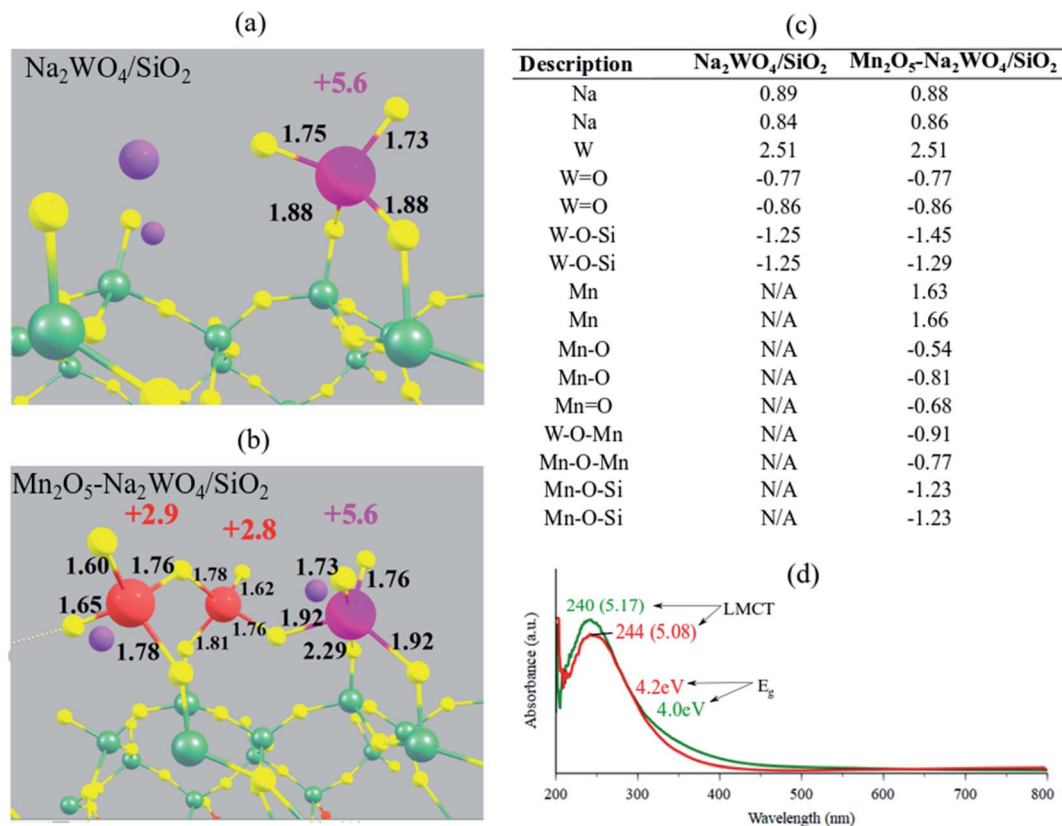


Fig. 5 Structural visualization of (a)  $\text{Na}_2\text{WO}_4/\text{SiO}_2$  and (b)  $\text{Mn}_2\text{O}_5\text{-Na}_2\text{WO}_4/\text{SiO}_2$  with calculated oxidation states mentioned next to the transition metal atoms in corresponding colors (Mn: red, W: pink). Oxidation states were calculated using a calibrated-fit for Bader charges, shown in Fig. S2 in the ESI section.<sup>†</sup> Calculated Bader charges for the surface sites in each case are summarized in table (c). (d) *In situ* dehydrated UV-Vis DRS of  $\text{Na-WO}_x/\text{SiO}_2$  (red) and  $\text{Mn-Na-WO}_x/\text{SiO}_2$  (green) catalysts, with  $E_g$  values and LMCT positions marked.



energies ( $\sim 240$  nm or 5.1 eV) indicate that W centers were indeed fully oxidized, *i.e.* +6, in agreement with the DFT results.<sup>22,50,51</sup> The edge energy ( $E_g$ ), indicative of the degree of polymerization of surface sites was  $\sim 4.2$  eV for Na-WO<sub>x</sub>/SiO<sub>2</sub> catalyst, but decreased to 4.0 eV upon Mn-promotion of Na-WO<sub>x</sub> sites, suggesting Mn-promotion increases polymerization in surface sites. The oxidation state of Mn atoms, on the other hand, cannot be determined from UV-vis DRS as UV-Vis DRS due to the low concentration of Mn in the Mn-Na-WO<sub>x</sub>/SiO<sub>2</sub> representative sample and the lower extinction coefficient of MnO<sub>x</sub> vs. WO<sub>x</sub>, the LMCT and d-d bands from Mn centers are masked by the absorbance of W sites.

The  $E_g$  value after Mn-promotion of Na-WO<sub>x</sub> sites is lower than the  $E_g$  value in the Na-WO<sub>x</sub> case (Fig. 5d), which can be further understood *via* density of states (DOS) analysis of DFT-optimized structures. Total DOS plots are shown in Fig. 6a and b for Na<sub>2</sub>WO<sub>4</sub>/SiO<sub>2</sub> and Mn<sub>2</sub>O<sub>5</sub>-Na<sub>2</sub>WO<sub>4</sub>/SiO<sub>2</sub>, respectively. For the Na<sub>2</sub>WO<sub>4</sub>/SiO<sub>2</sub> case, the valence band is primarily composed of occupied O 2p and W 5d states, while the conduction band of empty W 5d states. The energy gap between the top of the valence edge and the bottom of the conduction edge is  $\sim 1.7$  eV. However, in the Mn<sub>2</sub>O<sub>5</sub>-Na<sub>2</sub>WO<sub>4</sub>/SiO<sub>2</sub> case, the valence and conduction bands are primarily composed of Mn 3d states, with some contribution from occupied O 2p states in the valence band. In this case, the lowest part

of the conduction band lowers due to low-lying unoccupied Mn 3d states, reducing the bandgap to  $\sim 0$  eV. The DOS analysis shows that Mn-addition fundamentally changes the electronic structure of the surface sites by introducing low-lying vacant Mn 3d states above the Fermi level, which will have strong implications for the catalytic CH<sub>4</sub> activation. Elsewhere, it has been found that low-lying empty d states in a transition metal like Pt can act an acceptor for  $\sigma$ -donation from the C-H bond of CH<sub>4</sub> and lead to facile C-H scission.<sup>52</sup> Thus, it suffices to conclude at this point that experimental *in situ* UV-Vis DRS and computational DOS analysis are in qualitative agreement evidencing that Mn-promotion of Na<sub>2</sub>WO<sub>4</sub> surface sites will lower the  $E_g$  values due to the introduction of low-lying empty Mn 3d states above the Fermi level, that Mn is present in its +3 oxidation state, and that W is present in its fully oxidized +6 state.

#### (d) Reaction kinetics of CH<sub>4</sub> dissociation over Mn<sub>2</sub>O<sub>5</sub>-Na<sub>2</sub>WO<sub>4</sub>/SiO<sub>2</sub> vs. Na<sub>2</sub>WO<sub>4</sub>/SiO<sub>2</sub>

AITD analysis identified Mn<sub>2</sub>O<sub>5</sub>-Na<sub>2</sub>WO<sub>4</sub> as the most stable species under OCM relevant temperature and oxygen partial pressure. Therefore, the intrinsic activity of Na<sub>2</sub>WO<sub>4</sub>/SiO<sub>2</sub> vs. Mn<sub>2</sub>O<sub>5</sub>-Na<sub>2</sub>WO<sub>4</sub>/SiO<sub>2</sub> surface sites for CH<sub>4</sub> dissociation were studied, where the C-H bond dissociation is the most kinetically relevant elementary step in the OCM mechanism.<sup>19,53</sup> To

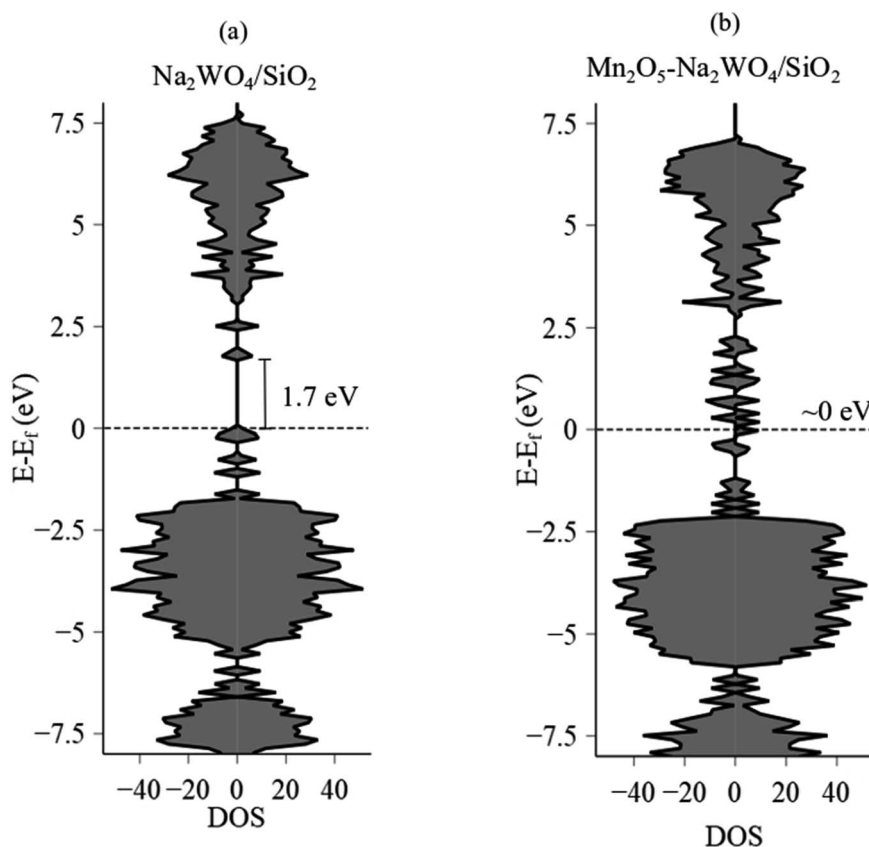
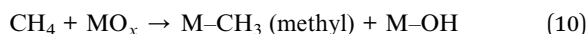
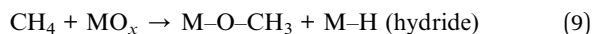


Fig. 6 Total electronic density of states (total DOS) and calculated band gap values (eV) for (a) Na<sub>2</sub>WO<sub>4</sub>/SiO<sub>2</sub> and (b) Mn<sub>2</sub>O<sub>5</sub>-Na<sub>2</sub>WO<sub>4</sub>/SiO<sub>2</sub>.  $E_F$  values for Na<sub>2</sub>WO<sub>4</sub>/SiO<sub>2</sub> and Mn<sub>2</sub>O<sub>5</sub>-Na<sub>2</sub>WO<sub>4</sub>/SiO<sub>2</sub> were  $-3.08$  eV and  $-2.75$  eV, respectively. The positive x-axis values correspond to spin-up, while the negative values correspond to spin-down states.



enhance readability and comprehension, the various possible reaction pathways for heterolytic C–H scission of CH<sub>4</sub> are grouped based on the type of surface intermediate formed in the forward step. Specifically,



where MO<sub>x</sub> represents a reactive metal oxide surface site (Mn<sub>2</sub>O<sub>5</sub> or WO<sub>4</sub>). In each case, the surface intermediate pair formed from CH<sub>4</sub> dissociation is unique, *i.e.* methoxy–hydroxy (OCH<sub>3</sub>, OH) in the red pathway, methoxy–hydride (OCH<sub>3</sub>, H) in the blue pathway and methyl–hydroxy (CH<sub>3</sub>, OH) in the green pathway, as shown in Fig. 7 and 9.

CH<sub>4</sub> dissociation over Na<sub>2</sub>WO<sub>4</sub> surface sites was studied as a function of the possible pathways listed above, and as a function of various active oxygen atoms. The results are summarized in Fig. 7a–c, highlighting the activation barriers associated with various possible pathways over the Na<sub>2</sub>WO<sub>4</sub>/SiO<sub>2</sub> catalyst. According to the computed energy barriers summarized in Fig. 7a, the highest energy barrier was for the pathway yielding OCH<sub>3</sub>, OH surface intermediates (3.4 eV), indicating that CH<sub>4</sub> dissociation turnover frequency for this pathway will be lower than other pathways with smaller transition state barriers. The two pathways with OCH<sub>3</sub>, H intermediates formation differ in terms of the oxygen atom of the WO<sub>4</sub> where C–H scission occurs, and consequently have slightly varying TS barriers (1.6, 1.9 eV). Lastly, the pathway yielding

CH<sub>3</sub>, OH surface intermediates exhibited the lowest energy barrier of 1.1 eV, suggesting that this is the dominant reaction pathway for CH<sub>4</sub> dissociation over Na-coordinated WO<sub>4</sub> surface sites in the Na<sub>2</sub>WO<sub>4</sub>/SiO<sub>2</sub> catalysts. The resulting intrinsic rate constants, calculated according to eqn (7) are plotted in Fig. 7b, suggesting that the intrinsic rate constant for the CH<sub>3</sub>, OH pathway is 2–3 orders of magnitude higher than other pathways making this the dominant pathway. Lastly, the initial, transition state (TS) and final structures for CH<sub>4</sub> activation over Na<sub>2</sub>WO<sub>4</sub> surface sites *via* the dominant reaction pathway are shown in Fig. 7c, showing the formation of W–CH<sub>3</sub> and W–O–H intermediates. Importantly, these results show that Na<sub>2</sub>WO<sub>4</sub> surface sites can effectively dissociate CH<sub>4</sub> in the absence of Mn-promoter in agreement with a recently published report,<sup>22</sup> as opposed to Lunsford<sup>19</sup> reaction model where Na–O–Mn sites are assumed to be the critical active sites for CH<sub>4</sub> dissociation.

Local DOS (LDOS) analysis was conducted to elucidate the changes in electronic structure of initial *versus* the TS structure during CH<sub>4</sub> dissociation over the Na<sub>2</sub>WO<sub>4</sub> surface sites. LDOS for W 5d states and O 2p states of the initial Na<sub>2</sub>WO<sub>4</sub> structure are shown in Fig. 8a. The valence band (below the Fermi level, E<sub>F</sub>) is comprised largely of occupied 2p states from the double-bonded oxygen *i.e.* W=O, while the conduction band is comprised largely of unoccupied W 5d states with a minor contribution from unoccupied O 2p states of W=O. Upon CH<sub>4</sub> dissociation, the lowest part of the conduction band lowers in energy as the unoccupied O 2p states get filled. Moreover, significant overlap of occupied states is observed for W 5d and C 2p states near the top of the valence edge at *ca.* –1.7 eV, signifying W–C bond formation as in the W–CH<sub>3</sub> surface intermediate. Lastly, occupied H 1s states and occupied O 2p

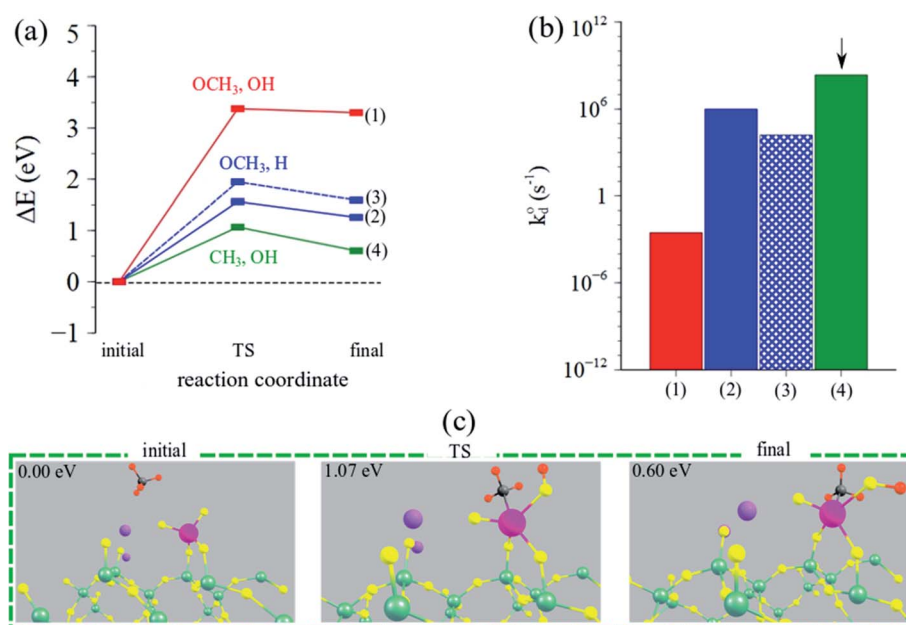


Fig. 7 (a) Reaction coordinate vs.  $\Delta E_{\text{DFT}}$  (eV) and (b) calculated intrinsic rate constants (log-scale) for CH<sub>4</sub> dissociation for the three possible pathways over the Na<sub>2</sub>WO<sub>4</sub>/SiO<sub>2</sub> catalyst. Arrow indicates the dominant (fastest) pathway. (c) Structural depictions of the initial, TS and final states during CH<sub>4</sub> dissociation over Na<sub>2</sub>WO<sub>4</sub>/SiO<sub>2</sub> catalysts yielding methyl–hydroxy (CH<sub>3</sub>, OH) intermediates. Pictorial summary for other pathways can be found in Table S3.†



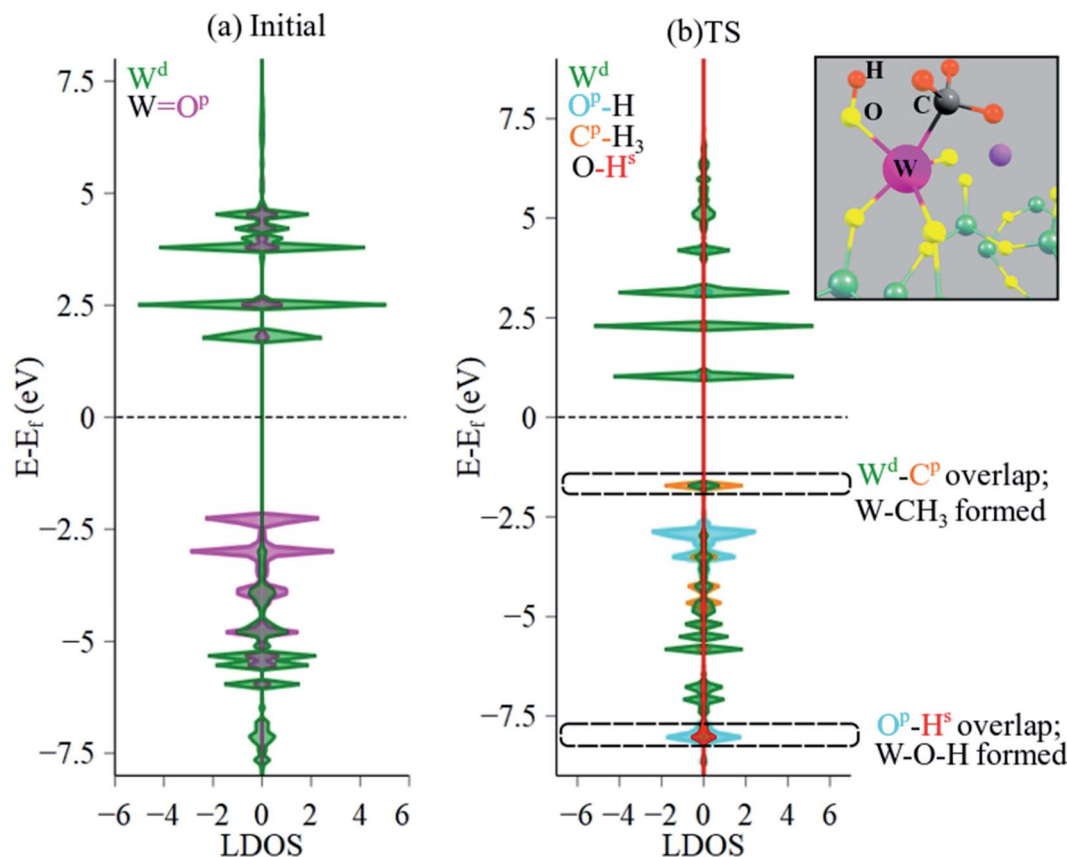


Fig. 8 LDOS analysis of (a) initial and (b) TS structures evidencing W-CH<sub>3</sub> and W-O-H formation, suggesting that CH<sub>4</sub> dissociation is mediated by a TS where a methyl is coordinated to the W center, while H is abstracted by W=O to form W-O-H. The inset shows the zoomed-in structure of the Na<sub>2</sub>WO<sub>4</sub> surface site with the pertinent atoms labeled.  $E_f$  for the initial structure was -3.08 eV and for the TS was -2.90 eV. Colored atoms correspond to the corresponding color in DOS plots.

states also overlap in the lower part of the valence edge, confirming O-H bond formation *i.e.* W-O-H intermediate. The Bader charge for W barely decreases; it changes from +2.51 in initial structure to +2.48 in the TS structure, indicating minimal reduction of the W center. The partial reduction of W center instead of a full reduction to +5 or to +4 might be the reason that reduced W centers could not be observed during OCM in SQUID-EPR experimentally.<sup>26</sup> Interestingly, a similar CH<sub>4</sub> dissociation pathway yielding CH<sub>3</sub>, OH surface intermediates was also proposed for La<sub>2</sub>O<sub>3</sub>-based catalysts, where La-CH<sub>3</sub> and La-O-H intermediates formed upon heterolytic dissociation of CH<sub>4</sub>.<sup>54</sup> Likewise, CH<sub>4</sub> dissociation over Al<sub>2</sub>O<sub>3</sub> was also shown to proceed *via* Al-CH<sub>3</sub> and Al-O-H formation.<sup>55</sup>

Next, intrinsic kinetics of CH<sub>4</sub> dissociation over Mn<sub>2</sub>O<sub>5</sub>-Na<sub>2</sub>WO<sub>4</sub>/SiO<sub>2</sub> catalyst were studied to ascertain if CH<sub>4</sub> still dissociated over the WO<sub>x</sub> like it did in the case of Na<sub>2</sub>WO<sub>4</sub>/SiO<sub>2</sub> catalyst. Once again, the color-coded pathways signify the unique surface intermediates produced. In this case however, CH<sub>4</sub> dissociation was studied as a function of the moiety since three distinct moieties are present in the surface site *i.e.* WO<sub>5</sub> moiety, W-O-Mn moiety, and Mn<sub>2</sub>O<sub>5</sub> moiety. The motivation behind studying CH<sub>4</sub> dissociation as a function of moieties is and to ascertain the affect of Mn<sub>2</sub>O<sub>5</sub> promotion on the reaction pathway and intrinsic kinetics. If, CH<sub>4</sub> dissociates preferentially

over the Mn<sub>2</sub>O<sub>5</sub> moiety, it would indicate that the effect of Mn-promotion in OCM catalysts is not to tune the WO<sub>x</sub> surface site but in fact to generate a second active site altogether. On the other hand, if it still activates over WO<sub>5</sub> moiety, the role of Mn<sub>2</sub>O<sub>5</sub> would be inferred as a structural/chemical promoter.

As shown in Fig. 9a, CH<sub>4</sub> dissociation becomes energetically unfavorable over the WO<sub>5</sub> moiety *i.e.* 2-4 eV TS barriers, in stark contrast to facile CH<sub>4</sub> dissociation observed over WO<sub>4</sub> site in Na<sub>2</sub>WO<sub>4</sub>/SiO<sub>2</sub> without Mn<sub>2</sub>O<sub>5</sub> promotion (1.1 eV). The higher TS barriers in the case of WO<sub>5</sub> moiety in Mn<sub>2</sub>O<sub>5</sub>-Na<sub>2</sub>WO<sub>4</sub>/SiO<sub>2</sub> catalyst in comparison to the pseudo-*T<sub>d</sub>* WO<sub>4</sub> moiety in Na<sub>2</sub>WO<sub>4</sub>/SiO<sub>2</sub> catalyst are likely due to the loss of *T<sub>d</sub>* geometry of the WO<sub>x</sub> center upon Mn<sub>2</sub>O<sub>5</sub> promotion, where the *T<sub>d</sub>* WO<sub>4</sub> serves as a reaction site. The *T<sub>d</sub>* geometry of the WO<sub>4</sub> is often regarded as a critical requirement of the selective active site in OCM in various experimental studies,<sup>19,22,25,56-60</sup> and that notion finds support from the DFT results herein.

On the other hand, CH<sub>4</sub> can also dissociate over the W-O-Mn and Mn<sub>2</sub>O<sub>5</sub> moieties *via* various pathways with TS barriers in the 1-5 eV range, shown in Fig. 9b and c. Overall, however, the lowest barrier pathway was the one yielding methoxy-hydroxy (OCH<sub>3</sub>, OH) intermediates, over the Mn<sub>2</sub>O<sub>5</sub> moiety, with a TS barrier of 0.72 eV, which is 0.3 eV lower than the lowest TS barrier pathway for CH<sub>4</sub> activation over Na<sub>2</sub>WO<sub>4</sub>/SiO<sub>2</sub>



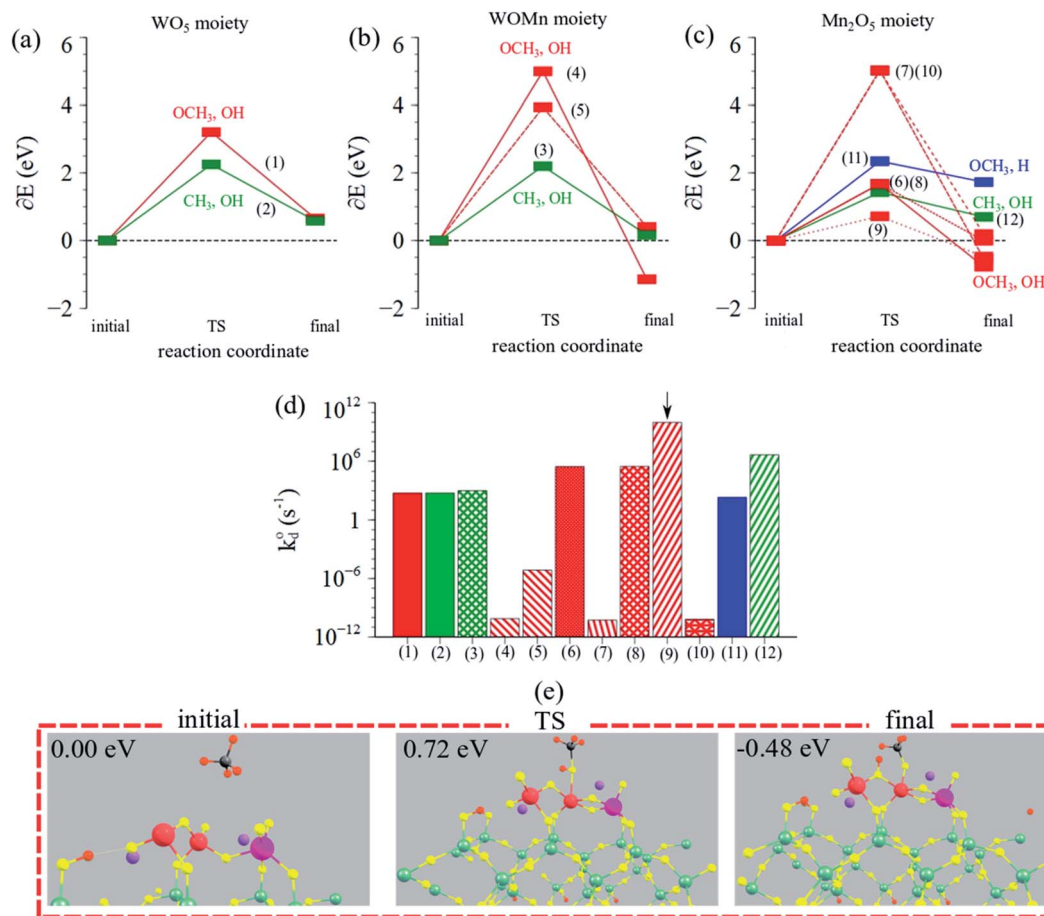


Fig. 9 Reaction coordinate vs.  $\Delta E_{\text{DFT}}$  (eV) over (a)  $\text{WO}_5$  moiety, (b)  $\text{W-O-Mn}$  moiety, (c)  $\text{Mn}_2\text{O}_5$  moiety in  $\text{Mn}_2\text{O}_5\text{-Na}_2\text{WO}_4/\text{SiO}_2$  catalyst. (d) Calculated intrinsic rate constants (log-scale) for  $\text{CH}_4$  dissociation for the possible pathways in  $\text{Mn}_2\text{O}_5\text{-Na}_2\text{WO}_4/\text{SiO}_2$  catalyst. Arrow indicates the dominant (lowest barrier) pathway. All numbered pathways 1–9 are described in ESI Table S4.† (e) Visualization of the dominant (lowest barrier) pathway for  $\text{CH}_4$  dissociation over the  $\text{Mn}_2\text{O}_5\text{-Na}_2\text{WO}_4/\text{SiO}_2$  catalyst, yielding methoxy–hydroxy ( $\text{OCH}_3$ ,  $\text{OH}$ ) surface intermediates.

in the absence of Mn-promoter. Fig. 9d compares the calculated intrinsic rate constants for  $\text{CH}_4$  dissociation across all moieties *via* various pathways studied, showing that the lowest TS barrier pathway indeed exhibits a rate constant orders of magnitude higher than other cases and hence is the dominant pathway. Lastly, initial, TS, and final structures for the dominant reaction pathway in this case are summarized in Fig. 9e, evidencing the involvement of Mn–O and Mn–O–Mn bonds in  $\text{CH}_4$  dissociation to yield Mn–O– $\text{CH}_3$  and  $(\text{Mn})_2\text{-O-H}$  surface intermediates.

To ascertain the electronic structural dynamics of the surface sites during  $\text{CH}_4$  dissociation, LDOS analysis (Mn 3d, O 2p, C 2p, H 1s states) was conducted for the initial and TS structures of  $\text{Mn}_2\text{O}_5\text{-Na}_2\text{WO}_4/\text{SiO}_2$ , shown in Fig. 10a and b, respectively. Initially, the valence edge is comprised of a mixture of occupied Mn 3d states and O 2p states from Mn–O–Mn and Mn–O bonds. The conductance edge is primarily made up of unoccupied Mn 3d states with some contribution from empty O 2p states. Upon  $\text{CH}_4$  dissociation and TS formation, the LDOS changes drastically. The upper part of the valence band lowers in energy, and occupied, spin-up Mn 3d states appear at  $-2.0$  eV, which were not present in the initial structure. Moreover, overlapping O 2p and C 2p states as well as the O 2p and H 1s states confirm

formation of Mn–O– $\text{CH}_3$  and  $(\text{Mn})_2\text{-O-H}$  intermediates. In this case, the occupied C 2p states overlap with occupied O 2p states of Mn–O towards the bottom of the valence edge ( $-7.0$  eV). Lastly, Mn Bader charge decreases from  $+1.63$  to  $+1.55$  from initial to TS structure, indicating reduction of the Mn centers from  $\sim+3$  to  $\sim+2$  in agreement with experimental literature.<sup>26,61</sup>

### (e) C–H bond activation over surface metal oxide sites

The results presented so far point out that heterolytic dissociation of  $\text{CH}_4$  can occur over surface sites, either  $\text{WO}_4$  or  $\text{Mn}_2\text{O}_5$ , *via* the Mars–van Krevelen (MvK) mechanism (*i.e.*, involvement of lattice oxygen instead of adsorbed  $\text{O}_2$ , as inferred from general agreement between TS barriers estimated herein and apparent activation barriers reported in the broader OCM literature in the  $100\text{--}150$   $\text{kJ mol}^{-1}$  range.<sup>19</sup> The dissociation of  $\text{CH}_4$  over pseudo- $T_d$   $\text{WO}_4$  sites in  $\text{Na}_2\text{WO}_4/\text{SiO}_2$  catalyst is found to be kinetically slower than that on  $\text{Mn}_2\text{O}_5$  moiety in  $\text{Mn}_2\text{O}_5\text{-Na}_2\text{WO}_4/\text{SiO}_2$  catalyst, given that the  $k_d^0$  value for C–H scission in  $\text{CH}_4$  over  $\text{Mn}_2\text{O}_5$  sites is 3 orders of magnitude higher than over the surface  $\text{Na}_2\text{WO}_4$  sites (Fig. 11). However, the formation of surface intermediates in the case of  $\text{CH}_4$  dissociation over



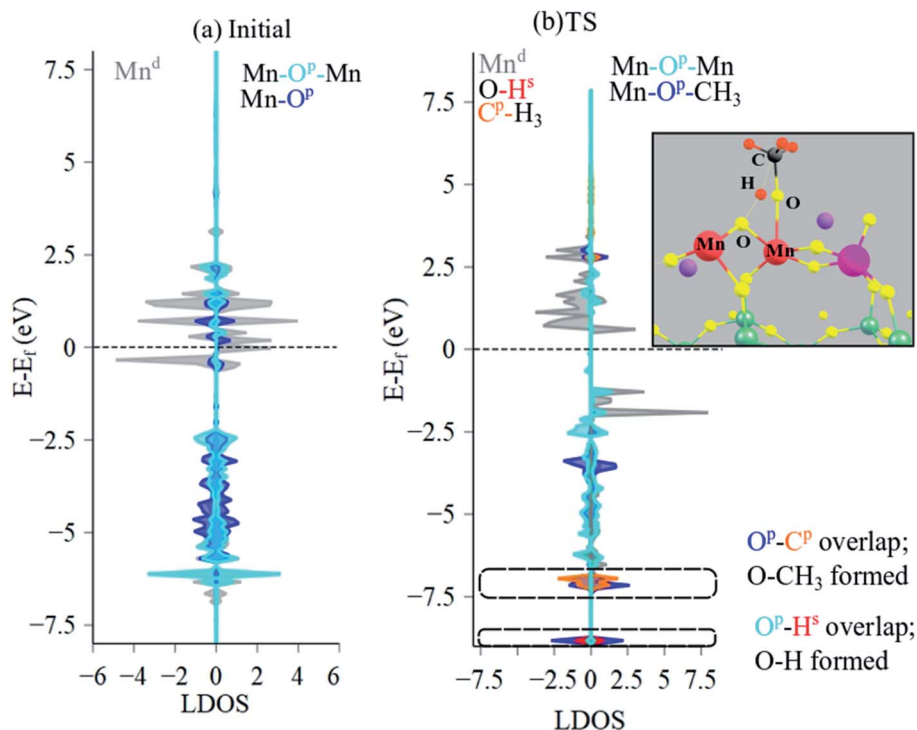


Fig. 10 LDOS analysis of (a) initial, and (b) TS structures, evidencing Mn–O–CH<sub>3</sub> and (Mn)<sub>2</sub>–O–H formation, suggesting that the CH<sub>4</sub> dissociation is mediated by a TS where a methyl is coordinated to the oxygens on the Mn center, while Mn–O–Mn bridging bond abstracts the hydrogen from the CH<sub>4</sub>.  $E_F$  value for the initial structure was  $-2.75$  eV and TS was  $-1.77$  eV. Colored atoms correspond to the corresponding color in DOS plots.

Na<sub>2</sub>WO<sub>4</sub> surface sites, namely W–CH<sub>3</sub> and W–O–H is endothermic by 0.60 eV. On the other hand, the formation of surface intermediates due to CH<sub>4</sub> dissociation over Mn<sub>2</sub>O<sub>5</sub> moiety in Mn<sub>2</sub>O<sub>5</sub>–Na<sub>2</sub>WO<sub>4</sub>/SiO<sub>2</sub>, namely Mn–O–CH<sub>3</sub> and Mn–O–H, is appreciably exothermic by  $-0.48$  eV. The occupied C 2p states of the CH<sub>3</sub> fragment in Mn–O–CH<sub>3</sub> are more stabilized (*i.e.*, lower in energy) when bound to Mn–O ( $-7.0$  eV) *vs.* when bound to W as in W–CH<sub>3</sub> ( $-1.7$  eV), as shown in Fig. 8 and 10, which

explains the enhanced stability of intermediates formed over Mn<sub>2</sub>O<sub>5</sub>. The higher stability of intermediates formed over Mn<sub>2</sub>O<sub>5</sub> moiety increases their likelihood of staying adsorbed and further oxidizing to the unselective CO<sub>x</sub> products instead of desorbing as methyl radicals into the gas-phase to form C<sub>2</sub> products.<sup>62</sup> It is known that the selectivity towards C<sub>2</sub> products in OCM relies on the thermodynamics of adsorption of the methyl fragment (ion or radical) on the catalyst, which can lead to further oxidation to CO or CO<sub>2</sub>.<sup>63</sup> Therefore, the energy of the adsorbed CH<sub>3</sub> fragment effectively describes the selectivity to C<sub>2</sub> hydrocarbons during the OCM process. Current results can be extrapolated to hypothesize slower kinetics of CH<sub>4</sub> dissociation, but higher C<sub>2</sub> selectivity for CH<sub>4</sub> dissociation over Na<sub>2</sub>WO<sub>4</sub> sites in Na<sub>2</sub>WO<sub>4</sub>/SiO<sub>2</sub> catalysts in comparison to CH<sub>4</sub> dissociation over Mn<sub>2</sub>O<sub>5</sub> sites in Mn<sub>2</sub>O<sub>5</sub>–Na<sub>2</sub>WO<sub>4</sub>/SiO<sub>2</sub>. In agreement with the present hypothesis, experimental results evidence higher CH<sub>4</sub> conversion, but lower C<sub>2</sub> selectivity for Mn–Na<sub>2</sub>WO<sub>4</sub>/SiO<sub>2</sub> (CH<sub>4</sub> conversion 36%, C<sub>2</sub> selectivity 54%) *vs.* Na<sub>2</sub>WO<sub>4</sub>/SiO<sub>2</sub> (CH<sub>4</sub> conversion 15%, C<sub>2</sub> selectivity 62%) catalysts in OCM.<sup>64</sup> A recent temporal analysis of products (TAP) reactor study of crystalline phase Mn–Na<sub>2</sub>WO<sub>4</sub>/SiO<sub>2</sub> catalysts further elucidated that the Na<sub>2</sub>WO<sub>4</sub>/SiO<sub>2</sub> catalyst (without Mn-oxide) possesses two distinct kinds of oxygen species at 800 °C: (i) a dissolved molecular O<sub>2</sub> type species only released from the molten Na<sub>2</sub>WO<sub>4</sub> phase and (ii) an atomic lattice O type species associated with surface Na–WO<sub>4</sub> sites that can be removed by reduction with CH<sub>4</sub>.<sup>65</sup> Both these oxygen species are catalytically active for the OCM reaction. On the other hand, the 1.2Mn/SiO<sub>2</sub> catalyst (without

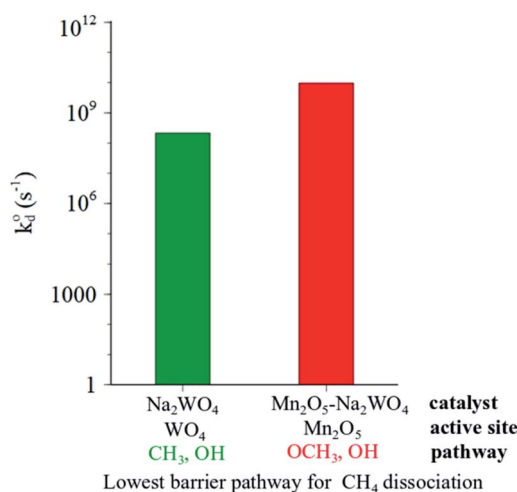


Fig. 11 Comparison of calculated intrinsic rate constants for dominant (lowest barrier) pathways for CH<sub>4</sub> dissociation over the Na<sub>2</sub>WO<sub>4</sub>/SiO<sub>2</sub> (green) and Mn<sub>2</sub>O<sub>5</sub>–Na<sub>2</sub>WO<sub>4</sub>/SiO<sub>2</sub> (red) catalysts.



$\text{Na}_2\text{WO}_4$ ) only provides molecular  $\text{O}_2$  type species associated with the Mn-oxide phase, and no atomic O type species. The  $\text{O}_2$  species associated with the Mn-oxide phase were found to be highly unselective toward  $\text{C}_2$  product formation from  $\text{CH}_4$  activation.<sup>65</sup> It would be interesting to conduct a similar TAP reactor study on model catalysts in the absence of crystalline oxide phases with only dispersed surface sites present to compare how such dispersed sites function *versus* the respective crystalline oxide phase.

The faster intrinsic kinetics of heterolytic  $\text{CH}_4$  dissociation over the  $\text{Mn}_2\text{O}_5$  sites *versus* the  $\text{Na}_2\text{WO}_4$  surface sites are not surprising. In fact, DFT calculations have been used to correlate the C–H bond activation energy to the surface reducibility (oxygen vacancy formation energy, work function) in the literature.<sup>63</sup> A linear correlation was found between the C–H activation energy and the oxygen vacancy formation energy of pure/doped metal-oxides, making surface reducibility a descriptor for predicting catalyst activity and selectivity for  $\text{CH}_4$  dissociation in OCM.<sup>63</sup> Given that Mn-oxides are more reducible than W-oxides, the  $\text{CH}_4$  dissociation over surface  $\text{Mn}_2\text{O}_5$  sites is expected to be faster than  $\text{Na}_2\text{WO}_4$ . Moreover, according to this correlation between C–H activation barrier and reducibility of the surface metal oxide site, one of the roles of Na-promotion is to increase the reducibility of surface  $\text{WO}_x$  sites, as evidenced by lowering of peak temperature values during  $\text{H}_2$ -TPR with Na-addition, reported in a recent study on  $\text{Na-WO}_x/\text{SiO}_2$  model catalysts.<sup>22</sup>

It is known that  $\text{MnO}_x$ -based catalysts form excellent partial and total oxidation catalysts owing to their enhanced reducibility. Examples of Mn-oxide based catalysts used for oxidation reactions include:  $\text{Mn}_2\text{O}_3$  for complete oxidation of methane,<sup>61</sup> Mn-oxide– $\text{CeO}_2$  catalysts for formaldehyde oxidation,<sup>66</sup> Spinel  $\text{CoMn}_2\text{O}_4$  for toluene oxidation,<sup>67</sup> mesoporous Mn-oxide catalysts for water oxidation,<sup>68</sup> alkane oxidation over Mn-perovskites,<sup>69</sup>  $\text{CeO}_2$ -supported Mn-oxide for propane oxidation,<sup>70</sup> In fact, analogous to the  $\text{CH}_4$  dissociation pathway over  $\text{Mn}_2\text{O}_5$  moiety envisioned in the present study, operando FTIR spectroscopy elsewhere<sup>71</sup> confirmed the formation of Mn–OH surface species by abstraction of hydrogen atoms by nucleophilic oxygen atoms (Mn–O–Mn) from propane during propane oxidation, providing support for the DFT modelling results and chemical insights presented herein.

Recent state-of-the-art understanding regarding the role of Mn- and Na-promoters in  $\text{Mn}_2\text{O}_3$ – $\text{Na}_2\text{WO}_4/\text{SiO}_2$  OCM catalysts puts chemical insights provided in the present work in perspective. Specifically, it was recently shown *via* experimental  $\text{CH}_4 + \text{O}_2$  temperature-programmed-surface-reaction of well-defined single site catalysts that  $\text{Na}_2\text{WO}_4$  surface sites could effectively and selectively activate  $\text{CH}_4$  in absence of any Mn-promoter to form  $\text{C}_2$  products, making the role of Mn-promoter unclear.<sup>22</sup> Further evidence of the dispersed phase Na– $\text{WO}_4$  surface sites being the critical OCM active sites was provided in recent experimental studies<sup>48,72</sup> where temporal analysis of products (TAP) reactor studies in conjunction with steady-state OCM reaction studies of  $\text{Na}_2\text{WO}_4/\text{SiO}_2$  catalysts (without Mn-oxide) demonstrated that the dispersed surface Na– $\text{WO}_4$  sites were responsible for selectively activating  $\text{CH}_4$  to

yield  $\text{C}_2$  and CO products, while molten  $\text{Na}_2\text{WO}_4$  phase was found to be mainly responsible for the over-oxidation of  $\text{CH}_4$  to  $\text{CO}_2$ , and oxidative dehydrogenation of  $\text{C}_2\text{H}_6$  to  $\text{C}_2\text{H}_4$ .<sup>72</sup> Likewise, Mn-containing phases including  $\text{MnO}_x$  surface oligomers,  $\text{MnWO}_4$  and Mn– $\text{WO}_3$  nanoparticles in Mn–Na– $\text{WO}_x/\text{SiO}_2$  tri-metal oxide model OCM catalyst were found to be primarily spectating during OCM under differential reaction conditions and when such Mn phases are present in small populations.<sup>48</sup> An older model study had previously shown that Na-coordinated  $\text{WO}_4$  surface sites were more selective but slightly less active than Mn-coordinated  $\text{WO}_x$  and uncoordinated  $\text{WO}_x$  sites during OCM in a series of model bi-metal oxide OCM catalysts.<sup>25</sup> Lastly, *via operando* synchrotron  $\mu$ -XRF/XRD/absorption-computed tomography, it was shown that crystalline manganese oxide phases including  $\text{Mn}_2\text{O}_3$ ,  $\text{Mn}_7\text{SiO}_{12}$  and  $\text{MnWO}_4$  are not required components to yield an active catalyst,<sup>6</sup> while no conclusion could be reached regarding the dispersed phase  $\text{Mn}_a\text{O}_b$  surface sites that can be present on the  $\text{SiO}_2$ .<sup>30</sup>

The current study, utilizing *in situ* spectroscopy, *ab initio* molecular dynamics, *ab initio* thermodynamics, and periodic-DFT modelling bridges the knowledge gap present in the literature and provides the following critical mechanistic insights, which suggest that Mn-promotion in fact is likely not essential for a yielding a selective-active OCM catalyst:

(1)  $\text{CH}_4$  heterolytically dissociates effectively over the  $\text{Na}_2\text{WO}_4$  surface sites in absence of Mn-promoter, with a TS barrier of 1.07 eV forming W– $\text{CH}_3$  and W–O–H surface intermediates. The surface intermediate formation is endothermic by 0.60 eV, indicative of their instability and likelihood of facile desorption.

(2)  $\text{CH}_4$  heterolytically dissociates over the  $\text{WO}_5$  moiety significantly slower when the  $\text{Mn}_2\text{O}_5$ – $\text{Na}_2\text{WO}_4/\text{SiO}_2$  catalyst is studied due to structural changes incurred upon  $\text{Mn}_2\text{O}_5$  coordination to the  $\text{WO}_4$  site forming the  $\text{WO}_5$ . This shows that Mn-promotion can in fact poison the otherwise pseudo- $T_d$   $\text{WO}_4$  surface active sites, retarding the kinetics of  $\text{CH}_4$  dissociation over them.

(3)  $\text{CH}_4$  dissociates over the  $\text{Mn}_2\text{O}_5$  moiety with a TS barrier of 0.72 eV forming Mn–O– $\text{CH}_3$  and (Mn)<sub>2</sub>–O–H surface intermediates. The surface intermediates formation is appreciably exothermic (–0.48 eV), indicative of the high stability of the formed intermediates.

(4) The significantly higher stability of surface intermediates formed when  $\text{CH}_4$  dissociates over the  $\text{Mn}_2\text{O}_5$  moiety in  $\text{Mn}_2\text{O}_5$ – $\text{Na}_2\text{WO}_4/\text{SiO}_2$  catalyst *versus* the intermediates formed upon  $\text{CH}_4$  dissociation over the  $\text{Na}_2\text{WO}_4/\text{SiO}_2$  signifies the likelihood of the Mn–O– $\text{CH}_3$ , (Mn)<sub>2</sub>–O–H surface intermediates over-oxidizing to  $\text{CO}_x$ , in agreement with the higher  $\text{CH}_4$  conversion but lower  $\text{C}_2$  selectivity reported in the OCM literature for  $\text{MnO}_x/\text{SiO}_2$  catalysts.<sup>64</sup> Therefore, the selective-active sites for OCM are the Na-coordinated  $\text{WO}_4$  surface sites present in  $\text{Na}_2\text{WO}_4/\text{SiO}_2$  catalysts without Mn-promotion. Mn promotion can create a second set of Mn-based surface sites (like the surface  $\text{Mn}_2\text{O}_5$  sites) that are more active for  $\text{CH}_4$  dissociation than the  $\text{WO}_4$ -based sites, but less selective to  $\text{C}_2$  products due to the



unfavorable desorption of the reaction intermediates formed over  $\text{Mn}_2\text{O}_5$ .

(5) Computational results herein also suggest that  $\text{CH}_4$  activation *via* the MvK mechanism where the oxygen species involved in the reaction originate in the solid phase catalytic active site is quite possible. The DFT-calculated intrinsic barriers of the MvK type reaction pathways are in general agreement with the experimental apparent activation energy values reported in the literature, providing qualitative support for the possibility of the MvK mechanism prevailing during catalytic OCM. However, we note that only the heterolytic  $\text{CH}_4$  activation pathway is studied herein and the homolytic  $\text{CH}_4$  activation pathway over these surface sites will be addressed in a future study. Literature studies have shown that both heterolytic and homolytic activation of  $\text{CH}_4$  occurs during OCM, where both pathways yield  $\text{CH}_3$  radicals in the gas-phase.<sup>73,74</sup> Typically, homolytic pathways exhibit higher energy barriers than the heterolytic pathway<sup>55</sup> due to the stabilization of the  $\text{CH}_3$  fragment from surface interactions in the heterolytic pathway.

## 4. Conclusions

The study herein utilized *in situ* spectroscopy, AIMD, AITD, and periodic-DFT to provide unprecedented chemical insights regarding  $\text{CH}_4$  activation over  $\text{Na}_2\text{WO}_4/\text{SiO}_2$  versus  $\text{Mn}-\text{Na}_2\text{WO}_4/\text{SiO}_2$  catalysts. We report, for the first time, that Mn-promotion is not essential to tune the pseudo- $T_d$   $\text{WO}_4$  surface sites known to be active for OCM. Contrary to previous understanding, we show that Mn-promotion poisons the pseudo- $T_d$   $\text{Na}_2\text{WO}_4$  surface site, with the resulting surface  $\text{WO}_5$  site exhibiting retarded kinetics for  $\text{CH}_4$  activation. With Mn-promotion, however, new Mn-based surface sites ( $\text{Mn}_2\text{O}_5$  in this study) form that can activate  $\text{CH}_4$  faster than the  $\text{WO}_4$ -based surface sites. The surface intermediates formed during  $\text{CH}_4$  dissociation over the  $\text{Mn}_2\text{O}_5$  sites ( $\text{Mn}-\text{O}-\text{CH}_3$ ,  $(\text{Mn})_2-\text{OH}$ ) are more stable than those formed *via*  $\text{CH}_4$  dissociation over the  $\text{Na}_2\text{WO}_4$  site ( $\text{W}-\text{CH}_3$ ,  $\text{W}-\text{O}-\text{H}$ ), and prone to over-oxidation to  $\text{CO}_x$  due to the unfavorable desorption. Considering these insights that agree with recent state-of-the-art *in situ* and *operando* characterization studies, it is proposed that the addition of  $\text{MnO}_x$  does not promote the pseudo- $T_d$ , Na-coordinated  $\text{WO}_4$  sites where  $\text{CH}_4$  activates selectively (*i.e.*, essential selective active sites for OCM). The Mn-promotion likely creates a second set of active  $\text{MnO}_x$  surface sites that are more active for  $\text{CH}_4$  activation, but less  $\text{C}_2$  selective than the Na- $\text{WO}_4$  surface sites. These findings contradict Lunsford's OCM model, where the Na-O-Mn sites are hypothesized to be critically involved in the redox mechanism during OCM.<sup>75</sup> The results herein also do not completely agree with Li's OCM model, as  $\text{W}^{6+}$  is barely seen to reduce during  $\text{CH}_4$  dissociation step, while Li proposed that W reduces from +6 to +5/+4 during the  $\text{CH}_4$  dissociation step, and  $\text{Mn}_2\text{O}_3$  provides electron-coupled oxygen-spillover to re-oxidize the reduced W sites back to +6 oxidation state.<sup>76</sup> Lastly, note that the findings herein do not account for the crystalline nanoclusters/nanoparticles (<2–3 nm) of  $\text{MnWO}_4$  or Mn-contaminated  $\text{WO}_3$  which are present in the tri-metal oxide

model catalyst studied herein. The exact nature of these nanoclusters/nanoparticles is not understood presently and they can only be modelled accurately to generate structure–function relationships for OCM when their size, shape, surface composition, vacancy/defect density, *etc.* are well-characterized. It suffices to note here that crystalline  $\text{MnWO}_4$ , even when present, does not contribute significantly to OCM.<sup>29,30</sup>

Future investigations on the role of surface  $\text{MnO}_x$  sites during  $\text{CH}_4$  activation in well-defined catalysts should include  $\text{CH}_4 + \text{O}_2$  temperature-programmed surface reaction, steady state performance tests, isotope-switch experiments in temporal analysis of products (TAP) reactor, and computational analysis of the homolytic pathway for  $\text{CH}_4$  activation over the catalyst models generated in this study.

## Data availability

Relevant data is present in the ESI file.†

## Author contributions

DK and JB conducted all theoretical work. DK and SS conducted spectroscopy experiments. DK, JB, and IEW wrote the manuscript. All authors have agreed to the publication of this manuscript.

## Conflicts of interest

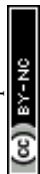
The authors declare no competing interests.

## Acknowledgements

This work is supported by NSF CBET 1706581. DK also gratefully acknowledges John C. Chen endowed fellowship for financial support. This work used the Extreme Science and Engineering Discovery Environment (XSEDE) (Comet cluster), which is supported by National Science Foundation grant number ACI-1548562, under allocation ID TG-CTS150038 with XSEDE.<sup>77</sup>

## References

- 1 X. Li, J. Xie, H. Rao, C. Wang and J. Tang, *Angew. Chem., Int. Ed.*, 2020, **59**, 19702–19707.
- 2 A. M. Arinaga, M. C. Ziegelski and T. J. Marks, *Angew. Chem., Int. Ed.*, 2021, **60**, 10502.
- 3 V. Paunović, G. Zichittella, M. Moser, A. P. Amrute and J. Pérez-Ramírez, *Nat. Chem.*, 2016, **8**, 803–809.
- 4 M. Moser, L. Rodríguez-García, A. P. Amrute and J. Pérez-Ramírez, *ChemCatChem*, 2013, **5**, 3520–3523.
- 5 A. Caballero and P. J. Perez, *Chem. Soc. Rev.*, 2013, **42**, 8809–8820.
- 6 M.-S. Salehi, M. Askarishahi, H. R. Godini, O. Görke and G. Wozny, *Ind. Eng. Chem. Res.*, 2016, **55**, 3287–3299.
- 7 T. N. Nguyen, T. T. P. Nhat, K. Takimoto, A. Thakur, S. Nishimura, J. Ohyama, I. Miyazato, L. Takahashi, J. Fujima, K. Takahashi and T. Taniike, *ACS Catal.*, 2020, **10**, 921–932.



- 8 Z. Cheng, D. S. Baser, S. G. Nadgouda, L. Qin, J. A. Fan and L.-S. Fan, *ACS Energy Lett.*, 2018, **3**, 1730–1736.
- 9 S. Parishan, P. Littlewood, A. Arinchtein, V. Fleischer and R. Schomäcker, *Catal. Today*, 2018, **311**, 40–47.
- 10 A. L. Tonkovich, R. W. Carr and R. Aris, *Science*, 1993, **262**, 221.
- 11 X. Guo, G. Fang, G. Li, H. Ma, H. Fan, L. Yu, C. Ma, X. Wu, D. Deng, M. Wei, D. Tan, R. Si, S. Zhang, J. Li, L. Sun, Z. Tang, X. Pan and X. Bao, *Science*, 2014, **344**, 616–619.
- 12 K. Takahashi, L. Takahashi, T. N. Nguyen, A. Thakur and T. Taniike, *J. Phys. Chem. Lett.*, 2020, **11**, 6819–6826.
- 13 L. Grajciar, C. J. Heard, A. A. Bondarenko, M. V. Polynski, J. Meeprasert, E. A. Pidko and P. Nachtigall, *Chem. Soc. Rev.*, 2018, **47**, 8307–8348.
- 14 P. Schlexer Lamoureux, K. T. Winther, J. A. Garrido Torres, V. Streibel, M. Zhao, M. Bajdich, F. Abild-Pedersen and T. Bligaard, *ChemCatChem*, 2019, **11**, 3581–3601.
- 15 J. A. Labinger, *Science*, 1995, **269**, 1833.
- 16 D. Kiani, S. Sourav, Y. Tang, J. Baltrusaitis and I. E. Wachs, *Chem. Soc. Rev.*, 2021, **50**, 1251–1268.
- 17 D. Kiani, G. Belletti, P. Quaino, F. Tielens and J. Baltrusaitis, *J. Phys. Chem. C*, 2018, **122**, 24190–24201.
- 18 R. K. Grasselli and A. W. Sleight, in *Studies in Surface Science and Catalysis*, ed. R. K. Grasselli and A. W. Sleight, Elsevier, 1991, vol. 67, p. ix.
- 19 D. Kiani, S. Sourav, J. Baltrusaitis and I. E. Wachs, *ACS Catal.*, 2019, **9**, 5912–5928.
- 20 Z. Li, S. Ji, Y. Liu, X. Cao, S. Tian, Y. Chen, Z. Niu and Y. Li, *Chem. Rev.*, 2020, **120**, 623–682.
- 21 L. Zhang, M. Zhou, A. Wang and T. Zhang, *Chem. Rev.*, 2020, **120**, 683–733.
- 22 D. Kiani, S. Sourav, I. E. Wachs and J. Baltrusaitis, *Catal. Sci. Technol.*, 2020, **10**, 3334–3345.
- 23 I. E. Wachs and K. Routray, *ACS Catal.*, 2012, **2**, 1235–1246.
- 24 S. Arndt, T. Otremba, U. Simon, M. Yildiz, H. Schubert and R. Schomäcker, *Appl. Catal., A*, 2012, **425–426**, 53–61.
- 25 D. Kiani, S. Sourav, W. Taifan, M. Calatayud, F. Tielens, I. E. Wachs, J. Baltrusaitis, I. E. Wachs and J. Baltrusaitis, *ACS Catal.*, 2020, **10**, 4580–4592.
- 26 W. Riedel, L. Thum, J. Möser, V. Fleischer, U. Simon, K. Siemensmeyer, A. Schnegg, R. Schomäcker, T. Risse and K.-P. Dinse, *J. Phys. Chem. C*, 2018, **122**, 22605–22614.
- 27 W. Pengwei, Z. Guofeng, Y. Wang, L. Yong, P. Wang, G. Zhao, Y. Wang and Y. Lu, *Sci. Adv.*, 2017, **3**, 1–10.
- 28 P. Wang, G. Zhao, Y. Liu and Y. Lu, *Appl. Catal., A*, 2017, **544**, 77–83.
- 29 M. J. Werny, Y. Wang, F. Girgsdies, R. Schlögl and A. Trunschke, *Angew. Chem., Int. Ed.*, 2020, **59**, 14921.
- 30 A. Vamvakeros, D. Matras, S. D. M. Jacques, M. di Michiel, S. W. T. Price, P. Senecal, M. A. Aran, V. Middelkoop, G. B. G. Stenning, J. F. W. Mosselmans, I. Z. Ismagilov and A. M. Beale, *J. Catal.*, 2020, **386**, 39–52.
- 31 H. Guesmi, R. Grybos, J. Handzlik and F. Tielens, *RSC Adv.*, 2016, **6**, 39424–39432.
- 32 K. Kurlito, F. Tielens and J. Handzlik, *J. Phys. Chem. C*, 2020, **124**(5), 3002–3013.
- 33 M. Lahti, A. Chaudhuri, K. Pussi, D. Hesp, I. M. McLeod, V. R. Dhanak, M. O. King, M. Kadodwala and D. A. MacLaren, *Surf. Sci.*, 2014, **622**, 35–43.
- 34 <http://www.p4vasp.at/>, 2021.
- 35 M. Yu and D. R. Trinkle, *J. Chem. Phys.*, 2011, **134**, 064111.
- 36 G. Henkelman, B. P. Uberuaga and H. Jónsson, *J. Chem. Phys.*, 2000, **113**, 9901–9904.
- 37 G. Henkelman and H. Jónsson, *J. Chem. Phys.*, 2000, **113**, 9978–9985.
- 38 G. Li, P. Vassilev, M. Sanchez-Sanchez, J. A. Lercher, E. J. M. Hensen and E. A. Pidko, *J. Catal.*, 2016, **338**, 305–312.
- 39 N. Kosinov, A. S. G. Wijkema, E. Uslamin, R. Rohling, F. J. A. G. Coumans, B. Mezari, A. Parastaev, A. S. Poryvaev, M. V. Fedin, E. A. Pidko and E. J. M. Hensen, *Angew. Chem.*, 2018, **130**, 1028–1032.
- 40 G. Li, I. Vollmer, C. Liu, J. Gascon and E. A. Pidko, *ACS Catal.*, 2019, **9**, 8731–8737.
- 41 *The Materials Project, Materials Data on Mn2O3 by Materials Project*, United States, 2014, DOI: 10.17188/1272415.
- 42 Y.-B. Kang and I.-H. Jung, *Metall. Mater. Trans. E*, 2016, **3**, 156–170.
- 43 W. E. W. E. Taifan, T. Bučko and J. Baltrusaitis, *J. Catal.*, 2017, **346**, 78–91.
- 44 M. W. Chase Jr, *NIST-JANAF thermochemical tables*, American Chemical Society, American Institute of Physics for the National Institute of Standards and Technology, Washington, DC, New York, 4th edn, 1998.
- 45 K. K. Irikura, *J. Phys. Chem. Ref. Data*, 2007, **36**, 389–397.
- 46 K. Reuter and M. Scheffler, *Phys. Rev. B*, 2001, **65**, 035406.
- 47 R. Jutta and K. Reuter, *Max-Planck-Gesellschaft Zur Foerderung Der Wissenschaften ev Berlin (GERMANY FR)*, Fritz-Haber-INST, 2006.
- 48 D. Kiani, S. Sourav, J. Baltrusaitis and I. E. Wachs, *ACS Catal.*, 2021, **11**, 10131–10137.
- 49 F. Yang, J. Graciani, J. Evans, P. Liu, J. Hrbek, J. F. Sanz and J. A. Rodriguez, *J. Am. Chem. Soc.*, 2011, **133**, 3444–3451.
- 50 E. I. Ross-medgaarden and I. E. Wachs, *J. Phys. Chem. C*, 2007, **111**, 15089–15099.
- 51 S. Lwin, Y. Li, A. I. Frenkel and I. E. Wachs, *ACS Catal.*, 2016, **6**, 3061–3071.
- 52 Q. Wan, V. Fung, S. Lin, Z. Wu and D.-e. Jiang, *J. Mater. Chem. A*, 2020, **8**, 4362–4368.
- 53 K. Takanabe and E. Iglesia, *J. Phys. Chem. C*, 2009, **113**, 10131–10145.
- 54 Z. Liu, J. P. Ho Li, E. Vovk, Y. Zhu, S. Li, S. Wang, A. P. van Bavel and Y. Yang, *ACS Catal.*, 2018, **8**, 11761–11772.
- 55 M. C. Cholewinski, M. Dixit and G. Mpourmpakis, *ACS Omega*, 2018, **3**, 18242–18250.
- 56 J. Wu, S. Li, J. Niu and X. Fang, *Appl. Catal., A*, 1995, **124**, 9–18.
- 57 S.-f. Ji, T.-c. Xiao, S. S.-B. B. Li, C.-z. Xu, R.-l. Hou, K. S. Coleman, M. L. H. Green, J. Wu, S. S.-B. B. Li, Z. C. Jiang, C. J. Yu, X. P. Fang, S. S.-B. B. Li, H. L. Wang, J. Wu, S. S.-B. B. Li, J. Niu, X. P. Fang, D. J. Wang, M. P. Rosynek, J. H. Lunsford, S. S.-B. B. Li, A. Palermo, J. Pedro, H. Vazquez and R. M. Lambert, *Appl. Catal., A*, 1995, **68**, 191–196.



- 58 J. Wu and S. Li, *J. Phys. Chem.*, 1995, **99**, 4566–4568.
- 59 S. Ji, T. Xiao, S. Li, L. Chou, B. Zhang, C. Xu, R. Hou, A. P. E. E. York and M. L. H. H. Green, *J. Catal.*, 2003, **220**, 47–56.
- 60 S. Li, *J. Nat. Gas Chem.*, 2003, **12**, 1–9.
- 61 Y.-F. Han, K. Ramesh, L. Chen, E. Widjaja, S. Chilukoti and F. Chen, *J. Phys. Chem. C*, 2007, **111**, 2830–2833.
- 62 M. J. Capitan, J. A. Odriozola, A. Marquez and J. F. Sanz, *J. Catal.*, 1995, **156**, 273–278.
- 63 G. Kumar, S. L. J. Lau, M. D. Krcha and M. J. Janik, *ACS Catal.*, 2016, **6**, 1812–1821.
- 64 S. Hou, Y. Cao, W. Xiong, H. Liu and Y. Kou, *Ind. Eng. Chem. Res.*, 2006, **45**, 7077–7083.
- 65 S. Sourav, Y. Wang, D. Kiani, J. Baltrusaitis, R. R. Fushimi and I. E. Wachs, *ACS Catal.*, 2021, **11**, 10288–10293.
- 66 J. Quiroz, J.-M. Giraudon, A. Gervasini, C. Dujardin, C. Lancelot, M. Trentesaux and J.-F. Lamonier, *ACS Catal.*, 2015, **5**, 2260–2269.
- 67 C. Dong, Z. Qu, Y. Qin, Q. Fu, H. Sun and X. Duan, *ACS Catal.*, 2019, **9**, 6698–6710.
- 68 C.-H. Kuo, I. M. Mosa, A. S. Poyraz, S. Biswas, A. M. El-Sawy, W. Song, Z. Luo, S.-Y. Chen, J. F. Rusling, J. He and S. L. Suib, *ACS Catal.*, 2015, **5**, 1693–1699.
- 69 G. Koch, M. Hävecker, D. Teschner, S. J. Carey, Y. Wang, P. Kube, W. Hetaba, T. Lunkenbein, G. Auffermann, O. Timpe, F. Rosowski, R. Schlögl and A. Trunschke, *ACS Catal.*, 2020, **10**, 7007–7020.
- 70 H. Wang, H. Zhou, S. Li, X. Ge, L. Wang, Z. Jin, C. Wang, J. Ma, X. Chu, X. Meng, W. Zhang and F.-S. Xiao, *ACS Catal.*, 2020, **10**, 10559–10569.
- 71 X. Li, D. Teschner, V. Streibel, T. Lunkenbein, L. Masliuk, T. Fu, Y. Wang, T. Jones, F. Seitz, F. Girgsdies, F. Rosowski, R. Schlögl and A. Trunschke, *Chem. Sci.*, 2019, **10**, 2429–2443.
- 72 S. Sourav, Y. Wang, D. Kiani, J. Baltrusaitis, R. R. Fushimi and I. E. Wachs, *Angew. Chem., Int. Ed.*, 2021, **60**, 21502.
- 73 J. H. Lunsford, *Angew. Chem., Int. Ed. Engl.*, 1995, **34**, 970–980.
- 74 D. Dissanayake, J. H. Lunsford and M. P. Rosynek, *J. Catal.*, 1994, **146**, 613–615.
- 75 D. J. Wang, M. P. Rosynek and J. H. Lunsford, *J. Catal.*, 1995, **155**, 390–402.
- 76 S. Li, *J. Nat. Gas Chem.*, 2003, **12**, 1–9.
- 77 J. Towns, T. Cockerill, M. Dahan, I. Foster, K. Gaither, A. Grimshaw, V. Hazlewood, S. Lathrop, D. Lifka, G. D. Peterson, R. Roskies, J. R. Scott and N. Wilkins-Diehr, *Comput. Sci. Eng.*, 2014, **16**, 62–74.

